ANGULAR ANALYSIS OF A WIDE-BAND ENERGY HARVESTER BASED ON MUTUALLY PERPENDICULAR VIBRATING PIEZOELECTRIC BEAMS

Sohrab MirzaAbedini

Thesis Prepared for the Degree of

MASTER OF SCIENCE

UNIVERSITY OF NORTH TEXAS

December 2016

APPROVED:

Haifeng Zhang, Major Professor
Jincheng Du, Committee Member
Seifollah Nasrazadani, Committee Member
Zhenhai Xia, Committee Member
Andrey Voevodin, Chair of the Department of Material Science and Engineering
Costas Tsatsoulis, Dean of the College of Engineering
Victor Prybutok, Vice Provost of the Toulouse Graduate School

MirzaAbedini, Sohrab. *Angular Analysis of a Wide-Band Energy Harvester based on Mutually Perpendicular Vibrating Piezoelectric Beams.* Master of Science (Material Science and Engineering), December 2016, 64 pp., 3 tables, 44 figures, 31 numbered references.

The recent advancements in electronics and the advents of small scaled instruments has increased the attachment of life and functionality of devices to electrical power sources but at the same time granted the engineers and companies the ability to use smaller sources of power and batteries. Therefore, many scientists have tried to come up with new solutions for a power alternatives. Piezoelectric is a promising material which can readily produce continuous electric power from mechanical inputs. However, their power output is dependent upon several factors such as, system natural frequency, their position in the system, the direction of vibration and many other internal and external factors. In this research the working bandwidth of the system is increased through utilizing of two different piezoelectric beam in different directions. The dependency of output power with respect to rotation angle and also the frequency shift due to the rotation angle is studied.

ACKNOWLEDGEMENTS

At first, I would like say my thanks and gratitude to my wife Saeedeh and my parents, Bahram and Mahrokh who were very supportive and patient and without them I could not reach this point in life.

I would like to express my gratitude and appreciation to my advisor, Dr. Haifeng Zhang, for his support, patience, and encouragement throughout my graduate studies. His initiative, technical and scientific advice was essential to the completion of this dissertation and I would like to thank him for giving me the unlimited access to the smart material laboratory.

Furthermore, I would like to appreciate Dr. Suresh Kaluvan for his scientific and experimental support.

The members of the advisory committee were very kind to guide me in the correct direction dozens of times, my co-advisor and graduate advisor Dr. Jincheng Du, and associate chair of the department of engineering technology Dr. Seifollah Nasrazadani. I also would like to thank Dr. Zhenhai Xia from department of Material Science for accepting to be my committee member and review my thesis in a short time.

Last but not the least, I want to express my thanks to my helpful friend Amirhossein Bagheri and also to all other faculty members and Lab mates in the departments of Material Science, Engineering Technology and Mechanical Engineering.

TABLE OF CONTENTS

Page

LIST OF TABLES

LIST OF FIGURES

LIST OF NOTATIONS

ω	Frequency
L_b	Beam's Length
L_p	Piezoelectric's Length
t_p	Piezoelectric's thickness
t_b	Beam's thickness
S	Strain
s_{ij}	Constants of compliance matrix
m	mass
m_0	Tip mass
ρ	density
u	displacement
b, c	Width
σ	Stress
x_n	Neutral axis
E	Young modulus
V	Voltage
$\bar{\varepsilon}_{33}$	Stress dielectric constant
ε_{33}	Strain dielectric constant
k_{33}	Coupling factor
D_i	Electric displacement component
T_i	Traction vector component
E_i	Electric field component
d_{ij}	Piezoelectric constant
P	Electrical Power
Z_L	Impedance
θ	Rotation angle
M	Momentum
Q	Electrical charge
I	Electrical current

CHAPTER 1

INTRODUCTION

1.1. Background

Piezoelectricity is a well-known phenomenon which is discovered by brothers Pierre and Jacque Curie in 1880 and it is divided into two category of direct and indirect effect. In direct piezoelectricity by applying mechanical pressure to the material the movement of the internal positive and negative ions result in an external electrical output. In indirect effect, the imposed electrical current to the piezoelectric material makes the material to deform to compensate the change in its electric potential. The direct effect is the one category which is used in energy harvesting technology. This method of producing power has gotten more credibility during recent years, since newer devices and instruments have become smaller and less power consumer. Piezoelectric energy harvester is an appropriate power generator since it can be small and can produce a relatively good amount of voltage from mechanical deformation or vibration. These benefits have led many scientists and researchers to study and implement this material for new technologies.

1.2. PZT

Since in this thesis for a piezoelectric material a piezoceramic which is PZT-5A has been used, it is proper to give a short introduction about this material. The PZT stands for lead zirconate titanite with a chemical formula of Pb[ZrxTi1-x]O3. PZT is the most common and widely used synthetic piezoelectric ceramic material with a perovskite configuration. The Ti^{4+} ion is located at the center and when PZT is displaced it creates a dipole on each ends of the unit cell hence producing an electrical charge. PZT is originally manufactured in 1952 at Tokyo institute of technology 72 years after the discovery of piezoelectricity by

Curie brothers. The raw materials of lead, zirconium and titanium are weighed in correct proportions and are mixed through a wet milling (steeped into water). After that the mix will be heated up to high degrees which reaches to $1000\ ℃$ inside a very clean ceramic containers. At a certain degree the suitable phase is achieved. However, the PZT is still in powder form. The powders will be held together though a sintering process with a slurry binder and then dried and pressed to manufacture a desired shape.

1.3. Objectives

To turn around the capabilities of piezoelectric energy harvesters and to compensate its shortcoming on the short bandwidth, a new configuration is proposed and also to be more practical in industrial and real world locations where only one side of the sublayer is available, a single piezoelectric is used in place of a collocated patch or a bimorpher beam. Furthermore, the relation of output power to the rotation angle of the beam is measured.

1.4. Approach

In this thesis, an exact analytical procedure has been deployed to study the effect of angular position of a single piezoelectric beam in a mutually perpendicular configuration on power-frequency bandwidth. The single piezoelectric beam has a longer length with respect to its thickness. Therefore, it is appropriate to use Euler-Bernoulli beam theory [1]. The beam which is considered here has a single PZT ceramic which covers only a small length of the beam near the clamped-end. Therefore, in our analytical approach the beam is divided into two parts, where one part has piezoelectric and another part is the beam alone. The regular analytical method

used to solve these kinds of problems consider a general Euler equation and would solve the governing equation to reach the desired values. However, in this research the fundamental strain-stress equations are used to be solved for a range of frequencies and to show power production. Additionally, because of using only one single PZT, an asymmetry would form on the strain profile of the beam and also the neutral axis will not be exactly in the middle of the profile. Hence, the new neutral axis is also calculated.

The validation of the results has been done with two methods of finite element simulation and experiment. The experimental setup and configuration is exactly the same as the analytical model and their results are compared in this research.

CHAPTER 2

LITERATURE REVIEW

2.1. An Overview of Energy Harvesting Methods

The need for energy is a subject which would never be outdated. There is always a need for an energy source. Despite the fact that new devices need less power to work, in the past few decades this subject not only has not been abated but also increased dramatically. The new concept is that a power source should be continuous, dependable, serviceable and independent of replacement [2]. Engineers are trying to harvest energy from every possible renewable source which is normally wasted or dissipated. These sources can be wind energy, solar energy, thermal and mechanical movements. The wind energy technologies has grown fast in the recent years and are divided into two category of inland and offshore wind turbines. In a conference journal from national renewable energy laboratory lab the growth of wind energy harvesting utilization has been showed from 1980 to 2015 in United States [3]. The solar energy harvesting has also been studied rigorously. In a research by J. Tang et al the challenges facing this technology are names as maximizing photon absorption, efficient charge separation and effective utilization of separated charges [4]. For low-power energy sources Thermal and Mechanical inputs are more desirable. For the Thermal energy harvesting one of the main categories is the pyroelectric thermal energy harvesting. In pyroelectric energy harvesting the fluctuation between heating and cooling generates electricity. In a work by A. Cuadras et al the air current produces such a fluctuation [5] In this project our focus is on energy harvesting through mechanical energy which is one of the biggest available sources for low-power electronic devices such as sensors, antennas, display devices and even cell phones. There are vast numbers of applications and sources of mechanical power which grows day by day. In a researchby S.R Anton and H.A Sodano

several selected piezoelectric based energy harvesters is studied [6]. The mechanical vibration energy source could be machine produced, like vibration produced from rotation of an automobile tire [7] or vibrations of a railway produced from the train movement [8,9]. The energy can also be human produced [10], like the piezoelectric energy harvester which is placed in a shoe which produce electricity from the movement and pressure on the shoe sole. [11] Ambient and environment can also be a source of power for mechanical energy harvesting, like ocean waves [12] or wind [13]. Harvesting mechanical energy from wind energy has been the subject of many researches. In one study, energy is harvested from vortex induced by aeroelastic vibrations of the air [14]. In all these works piezoelectric is a material in which the conversion of energy is happening. In this project we also focused on piezoelectric material or more specifically the PZT (Lead-Zirconate-Titanite), $Pb[Zr_xTi_{1-x}]O_3$ which is one of the most commonly used material for energy harvesting. The recent effort and trend in energy harvesting though is to increase the working frequency which is explained more in the following.

2.2. Approaches to Increase Bandwidth

Working frequency is the frequency at which the energy harvester produces the maximum amount of power because of the matching between natural frequency of the system and the external simulation frequency. In a regular piezoelectric beam this point is limited to only one single frequency and therefore limiting the applicability of this type of energy harvester. Therefore, a mismatch between resonance frequency and natural frequency would cause a power loss in the energy harvester [15]. Many studies have been carried out to find a solution and many new configurations have been proposed. Some researchers use multiple piezoelectrics to increase the repetition of resonance frequency [16]. Many other scientific efforts have been

performed to increase the bandwidth including different setups and applying various boundary conditions. For a bimorph beam which stands for the use of two piezoelectric layer on a beam one research has been proposed connecting the two beams with a tip mass and a spring in between to be elastically and electrically connected in order to produce a wide bandwidth [17]. In another research the excitation itself has been changed to nonlinear which exploit stochastic resonance with white-noise excitation and also the use of a permanent magnet which is coupled to a piezoelectric beam in order to create a stable system [18]. As seen in this section, most of the projects are carried out for a bimorph or symmetrical collocated piezoelectric beam, in the following a brief review of the reasons for using bimorph or unimorph is discussed.

2.3. Unimorph or Single Piezoelectric

As mentioned previously the utilization of double piezoelectric layer, namely bimorph or double piezoelectric patch would create a symmetry in the strain profile which would make the governing equations easier [19]. However, whether this is always applicable in the real world or is the two side of a vibrating plate or beam always accessible is a subject that some researches took into account and proposed single piezoelectric as another available option. In Figure 2.1. Profile of the beam with single and double piezoelectricFigure 2.1a schematic of a single and double piezoelectric can be seen.

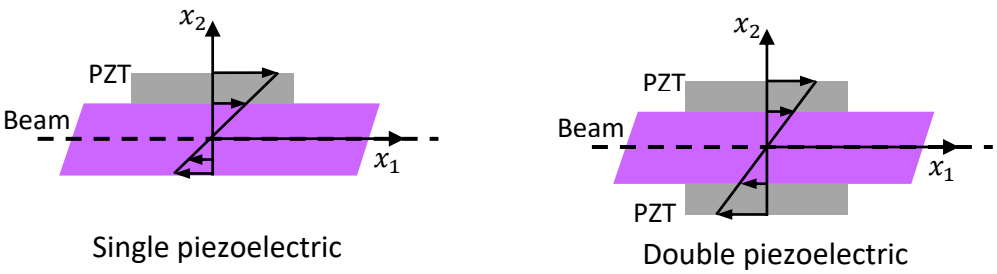

Figure 2.1. Profile of the beam with single and double piezoelectric

One important subject which should be considered here is the terminology of unimorph, bimorph and patch. The words unimorph and bimorph describe the cases where the piezoelectric parts are thin and can be referred as layer. If there is only one layer it is a unimorph and if there are two it would be bimorph. Piezoelectric patch usually refers to the application of a sensor and actuator at the same time on both side of the beam. In this thesis the PZT is thicker than a layer and that's why the usage of the term unimorph or layer has been avoided. Furthermore, that's another reason why there would be an asymmetry in the stress profile.

For a thin piezoelectric in a work by A. Erturk and D. Inman a unimorph piezoelectric beam has been analytically analyzed [20]. Also an array of unimorph piezoelectric beams has been used for a wide band width energy harvester. Which is a combination the approaches just covered up to this point [21]. The unimorph piezoelectric beam has been also used for nanoscale energy harvesting. In a work by Wang [22] a nanoscale beam with tip mass and base vibration has been modeled mathematically by the use of energy equations and Hamiltonian principle and in the end the amount of output voltage versus different frequencies and the effect of flexoelectricity has been studied. As it has been showed here most of the works are involved with piezoelectric layers which are regarded as a film on the substrate. The single piezoelectric beam has been studied by J. Zhao et al [23] in an analytical approach but the piezoelectric is covering the whole part of the beam. In our study the piezoelectric is nearly as thick as the beam and also it is covers the beam partially near the cantilevered end. Another aspect which has been studied in this research is the effect of rotation on power output which is discussed in the following.

2.4. Effect of Rotation on Power

In real world implementation of energy harvesters, the exact horizontal position is not always happening and in many places is also applicable. The effect of rotation angle on energy harvesters has been studied for different configurations. In a study by Peng Li et al a cubic beam with four piezoelectric layers has been studied and the effect of rotation on power output has been showed for different piezoelectric thicknesses [24]. Also in a similar work for a cubic beam four piezoelectric layers has been considered which have a shorter piezoelectric width comparing to the beam [25]. It is necessary to clarify that the beam is not rotating along an axis at all. The beam has only a deviation from its horizontal position around its longitudinal axis. Because in some researches the effect of rotation and velocity on an energy harvester is studied [26] and it should not be mistaken with the subject at hand. Furthermore, it should also be noted that the rotation is not going to produce a torsion stress in the beam which has been studied previously in a research to measure the amount of power in a coupled bending-torsion system [27].

CHAPTER 3

ANALYTICAL METHOD

3.1. Configuration and Setup

The two beams which are considered here are cantilevered into a fix support which would vibrate vertically in x_2 direction with an amplitude of A and frequency of ω.

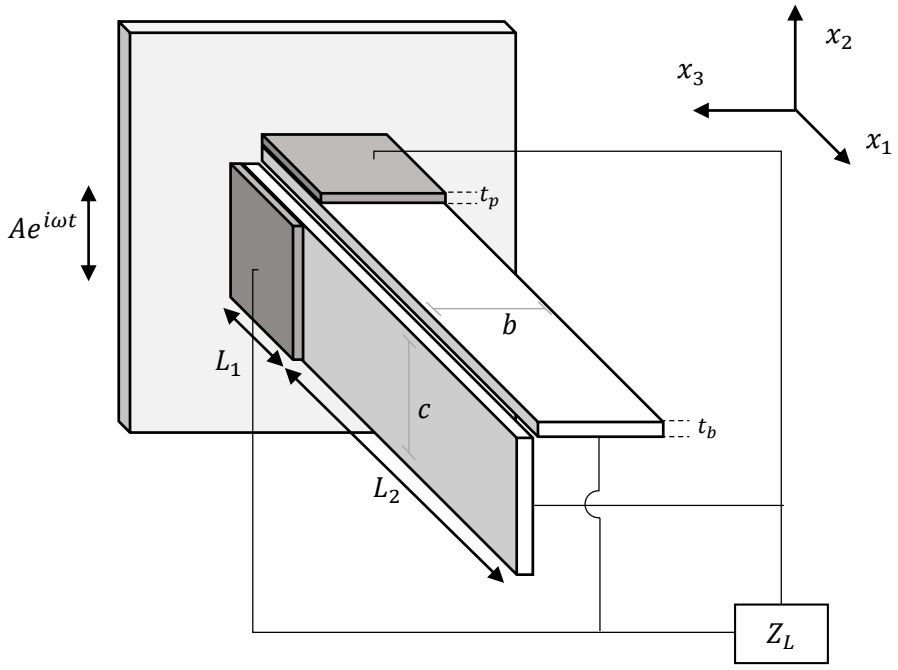

Figure 3.1. Schematic of the vibrating system

As it can be seen in the Figure 3.1, the piezoelectric patches are only on one side of the beam and close to the cantilevered end. The horizontal position is referred to the position which is along $x_3 - x_1$ plane and moving in x_2 direction. Also the vertical position is indicated by positioning in $x_2 - x_1$and moving in x_3 direction. It is important to know that the beams are not mechanically attached and there is only electrical connection between them. Therefore, there

would be enough gap between them to vibrate without hindrance. The beam motion is divided into two components to take the effect of rotation angle into account.

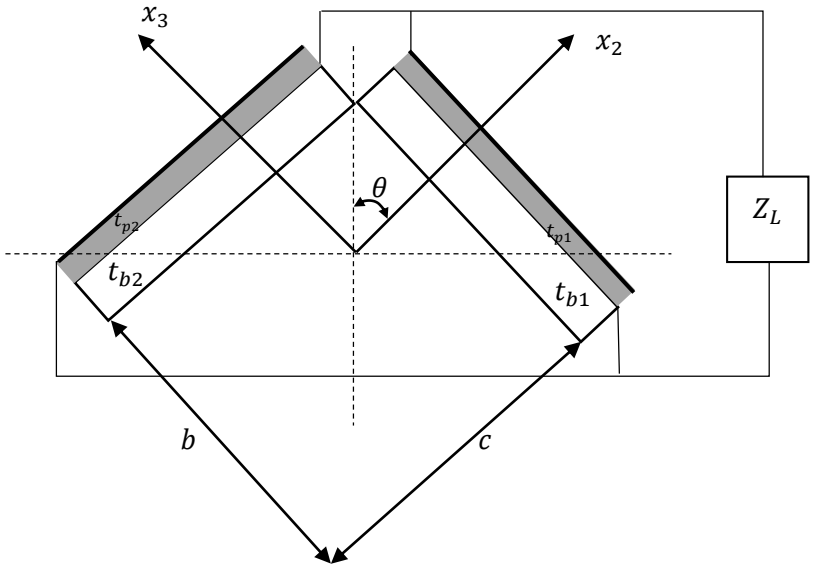

Figure 3.2. Profile of Both beams, movement Components and angles

Each beam has its own sets of equations and its own $x_2 - x_3$ components. As it can be seen in Figure 3.2 the beam thickness is noted with t_b and the piezoelectric thickness is displayed by t_p. The width of the first beam is shown with b and the second beam with c. As mentioned earlier, only one piezoelectric ceramic would create an asymmetry and the neutral axis would move from the middle position. Therefore it has to be calculated separately.

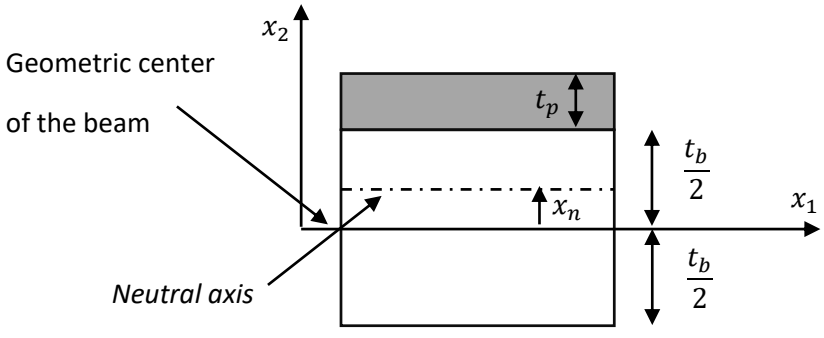

Figure 3.3. Profile of beam and piezoelectric, Neutral axis calculations

The neutral axis is displayed as x_n in figure 3.3. It is also noteworthy to mention that the thickness of beam and piezoelectric has been changed for the second beam. That is, there are two piezoelectrics of different thickness that are poled in their thickness direction and electroded on top of them. This is depicted in Figure 3.2 and Figure 3.3 by thick lines.

3.2. Circuitry

The outer electrodes are connected in series to each other and to an output circuit which its impedance is denoted by Z_L and is also depicted in Figure 3.1. Furthermore, in the opposite direction, the bottom electrodes of the piezoelectric patches are shorted and grounded as a reference.

3.3. Calculation of Neutral Axis

In the section of beam where the piezoelectric patch is attached $0 < x < L_1$, the material properties changes in the thickness direction. The neutral axis for asymmetrical strain profile which belongs to the bimorph or a collocated piezoelectric patch is in the middle of the profile. However, for this case the neutral axis would be placed above middle line as it can be seen in Figure 3.3 and it would be calculated as follows: [28]

$$S_1 = (x - x_n)u_{2,11} \tag{1}$$

Where x_n is the neutral axis. The sum of all forces along x_1 over the entire cross-section should be zero. Additionally, by applying Hook's law for strain-stress relation and summarization, we get:

$$b\int_{-\frac{t_b}{2}}^{\frac{t_b}{2}} \sigma_b(x_2)dx_2 + b\int_{\frac{t_b}{2}}^{\frac{t_b}{2}+t_p} \sigma_p(x_2)dx_2 = 0 \tag{2}$$

Where σ_b, σ_p are respectively stress induced in the beam and piezoelectric material section. By substituting the strain equation:

$$\int_{-\frac{t_b}{2}}^{\frac{t_b}{2}} E_b(x_2 - x_n)dx_2 + \int_{\frac{t_b}{2}}^{\frac{t_b}{2}+t_p} E_p(x_2 - x_n)dx_2 = 0 \quad (3)$$

E_b and E_p are the Young modulus of beam and piezoelectric respectively. By simplifying equation (3) we would have the neutral axis as follows:

$$x_n = \frac{E_p t_p(t_p + 2b)}{2(E_b t_b + E_p t_p)} \quad (4)$$

3.4. Stress-Strain Equations of the Beam and Piezoelectric

The Calculated neutral axis will be used later when the momentum over the entire beam is calculated. The axial normal strain component for the described beam model in x_2 and x_3 direction with flexural deflections of $u_2(x_1, t)$ and $x_3(x_1, t)$ is[24]:

$$S_1 = -x_2 u_{2,11} - x_3 u_{3,11} \quad (5)$$

The notation used here for subscript of u denotes number of partial differentiation in the desired direction, For example $u_{2,11}$ means $\partial^2 u_2 / \partial x_1^2$.

Therefore, the stress relation for the isotropic elastic beam is:

$$T_1 = E S_1 = -E(x_2 u_{2,11} + x_3 u_{3,11}) \quad (6)$$

E is the Young Modulus of Material. The electric field in the piezoelectric patch along the poling direction is denoted by E_3 and is given by:

$$E_3 = -V/t_p \tag{7}$$

Other components of electric field like E_1 and E_2 are equal to zero. V is the voltage across each piezoelectric patch, and t_p is the piezoelectric thickness. By considering the one-dimensional stress approximation of a beam with one nonzero component T_1, the constitutive relations for the anisotropic patch of piezoelectric are given by: [29]

$$\begin{aligned} S_1 &= s_{11}T_1 + d_{31}E_3 \\ D_3 &= d_{31}T_1 + \varepsilon_{33}E_3 \end{aligned} \tag{8}$$

s_{11} , ε_{33}, and d_{31} are respectively the elastic compliance, transverse dielectric constant, and the transverse-axial piezoelectric coefficient. D_3 is the transverse electric displacement. Equation (1) will be substituted in equation (4) and also inverted for the stress and electric displacement to get:

$$\begin{aligned} T_1 &= s_{11}^{-1}\left(-x_2u_{2,11} - x_3u_{3,11}\right) - s_{11}^{-1}d_{31}E_3 \\ D_3 &= d_{31}s_{11}^{-1}\left(-x_2u_{2,11} - x_3u_{3,11}\right) + \bar{\varepsilon}_{33}E_3 \end{aligned} \tag{9}$$

ε_{33} which is the strain dielectric constant is replaced by $\bar{\varepsilon}_{33}$ which is the stress dielectric constant to comply with units of equation (9) and it is equal to $\bar{\varepsilon}_{33} = \varepsilon_{33}(1 - k_{31}^2)$ and the coupling between electrical and mechanical field is $k_{33}^2 = d_{31}^2/(\varepsilon_{33}s_{11})$. [29]

The part of the beam which has a piezoelectric patch is assumed as the first part and has properties different from the second part which contains the beam alone. Therefore, each part is solved individually and then the total equilibrium conditions is superimposed.

The Momentum components for the first section of the first beam in x_2 and x_3 direction are:

$$
\begin{aligned}
M_{211} &= \int_S x_2\, T_1 dA \\
&= bE_b \int_{-x_n-\frac{t_b}{2}}^{\frac{t_b}{2}-x_n} x_2\left(-u_{2,11}x_2 - u_{3,11}x_3\right)dx_2 \\
&+ b \int_{\frac{t_b}{2}-x_n}^{\frac{t_b}{2}+t_p-x_n} x_2(s_{11}^{-1}\left(-u_{2,11}x_2 - u_{3,11}x_3 - E_3 d_{31}\right)dx_2 \\
&= D_{211}u_{2,11} + G_{211}(V) \\
M_{311} &= \int_S x_3\, T_1 dA \\
&= \left(t_b + t_p\right).E_b \int_{-\frac{b}{2}}^{\frac{b}{2}} -x_3\left(u_{2,11}x_2 + u_{3,11}x_3\right)dx_3 \;\; + (t_b \\
&+ t_p) \int_{-b/2}^{b/2} x_3(s_{11}^{-1}\left(-u_{2,11}x_2 - u_{3,11}x_3 - d_{31}E_l\right)dx_3 \\
&= D_{311}u_{3,11} + G_{311}(V)
\end{aligned}
\tag{10}
$$

For the beam section alone $l_1 < x_1 < l_2$, we have:

$$
\begin{aligned}
M_{221} &= -bE_b \int_{-\frac{t_b}{2}}^{\frac{t_b}{2}} x_2\left(u_{2,11}x_2 + u_{3,11}x_3\right)dx_2 = D_{221}u_{2,11} + G_{221}V \\
M_{321} &= -t_b E_b \int_{-b/2}^{b/2} x_3\left(u_{2,11}x_2 + u_{3,11}x_3\right)dx_3 = D_{321}u_{3,11} + G_{321}V
\end{aligned}
\tag{11}
$$

The subscript notation proposed here for *M*, *D*, and *G* which are respectively momentum, coefficients of $u_{2,11}$, $u_{3,11}$ and coefficients of E_3 are only for simplifying the many equations and are different from differentiation subscript used for deflection $u_{i,ijk}$. In this notation the first digit is for differentiation direction ($x_2\ or\ x_3$), the second number is for part number (part I (beam and

piezoelectric), part II (only beam)) and the third subscript is for the number of beams (beam 1 or 2). Therefore with this notation we have the followings from (10) and (11):

$$D_{211} = bE_b\left(-\frac{1}{3}\left(\frac{t_b}{2}-x_n\right)^3+\frac{1}{3}\left(-x_n-\frac{t_b}{2}\right)^3\right)-\frac{\frac{1}{3}b\left(\left(\frac{t_b}{2}+t_p-x_n\right)^3-\left(\frac{t_b}{2}-x_n\right)^3\right)}{S_{11}},$$

$$\begin{gathered} D_{311} = -\frac{1}{12}(t_b+t_p)b^3(E_b-S_{11}^{-1}), \\ D_{221} = \frac{1}{12}bE_bt_b^3, \\ D_{321} = \frac{2}{3}t_bE_bb^3. \\ G_{211} = bd_{31}s_{11}^{-1}(t_b+t_p-2x_n) \\ G_{311} = 0 \\ G_{221} = 0, \\ G_{321} = 0. \end{gathered} \tag{12}$$

As previously mentioned and denoted from equation (5), it must be taken into consideration that each section has its own x_2 and x_3 components. Therefore, there are 4 different momentum equations for each beam with 8 coefficients. For the second beam we have:

$$\begin{aligned} M_{312} &= \int_S x_3\,T_1\,dA \\ &= cE_b\int_{-x_n-\frac{t_b}{2}}^{\frac{t_b}{2}-x_n} x_3(-u_{2,11}x_2-u_{3,11}x_3)dx_3 \\ &+ c\int_{\frac{t_b}{2}-x_n}^{\frac{t_b}{2}+t_p-x_n} x_3(s_{11}^{-1}((-u_{2,11}x_2-u_{3,11}x_3-E_3d_{31})dx_3 = \\ &= D_{312}u_{3,11}+G_{312}(V) \end{aligned} \tag{13}$$

$$M_{212} = \int_S x_2\, T_1 dA =$$

$$= (t_b + t_p).\int_{-\frac{c}{2}}^{\frac{c}{2}} x_2(-u_{2,11}x_2 - u_{3,11}x_3)dx_2$$

$$+ \int_{-\frac{c}{2}}^{\frac{c}{2}} x_2(s_{11}^{-1}((-u_{2,11}x_2 - u_{3,11}x_3 - d_{31}E_3)dx_2$$

$$= D_{212}u_{3,11} + G_{212}(V)$$

$$M_{322} = -cE_b \int_{-\frac{t_b}{2}}^{\frac{t_b}{2}} x_3(u_{2,11}x_2 + u_{3,11}x_3)dx_3 = D_{322}u_{3,11} + G_{322}V$$

$$M_{222} = -cE_b \int_{-\frac{c}{2}}^{\frac{c}{2}} x_2(u_{2,11}x_2 + u_{3,11}x_3)dx_2 = D_{222}u_{3,11} + G_{222}V$$

In (13):

$$D_{312} = cE_b\left(-\frac{1}{3}\left(\frac{t_b}{2} - x_n\right)^3 + \frac{1}{3}\left(-x_n - \frac{t_b}{2}\right)^3\right) - \frac{\frac{1}{3}c\left(\left(\frac{t_b}{2} + t_p - x_n\right)^3 - \left(\frac{t_b}{2} - x_n\right)^3\right)}{S_{11}},$$

$$D_{212} = -\frac{1}{12}(t_b + t_p)c^3(E_b - S_{11}^{-1}),$$
$$D_{322} = \left(\frac{1}{12}\right)cE_b t_b^3, \qquad (14)$$

$$D_{222} = \left(\frac{2}{3}\right)t_b E_b c^3,$$

$$G_{312} = \frac{c}{2}d_{31}s_{11}^{-1}(t_b + t_p - 2x_n),$$
$$G_{212} = 0$$
$$G_{322} = 0,$$
$$G_{222} = 0.$$

The classical flexural motion equations of one angular slim beam of two sections are:

Beam 1

Section 1 for $0 < x_1 < L_1$:

$$M_{211,11} = m\ddot{u}_2, \qquad (15)$$
$$M_{311,11} = m\ddot{u}_3,$$

Section 2 for $L_1 < x_1 < L_2$: $M_{221,11} = m\ddot{u}_2$,
$M_{321,11} = m\ddot{u}_3$,

Beam 2

Section 1 for $0 < x_1 < L_1$: $M_{212,11} = m\ddot{u}_2$,
$M_{312,11} = m\ddot{u}_3$,

Section 2 for $L_1 < x_1 < L_2$: $M_{222,11} = m\ddot{u}_2$,
$M_{322,11} = m\ddot{u}_3$,

Where m is the general symbol for mass per unit length of the beam alone or beam and piezoelectric, we actually have:

Beam I or II: $m_{part\ I} = b\rho_b t_b + b\rho_p\, t_p$ $m_{part\ II} = b\rho_b t_b$ (16)

In the above equation, ρ_b is the mass density for beam and ρ_p belongs to piezoelectric respectively. The tip mass is indicated by m_0.

Recalling the constitutive relation from (8), the electric charges on the outer electrodes of the piezoelectric patches are:

$$\begin{aligned} Q_2 &= -\int_0^{L_1} dx_1 \int_{-c/2}^{c/2} D_3\big(x_2 = b + t_p\big)dx_3 \\ &= s_{11}^{-1} d_{31} c\big(b + t_p\big)\big[u_{2,1}(L_1) - u_{2,1}(0)\big] + \bar{\varepsilon}_{33}\frac{V}{t_p} cL_1 \\ Q_3 &= -\int_0^{L_1} dx_1 \int_{-b/2}^{b/2} D_3\big(x_3 = t_b + t_p\big)dx_2 \\ &= s_{11}^{-1} d_{31} b\big(t_b + t_p\big)\big[u_{3,1}(L_1) - u_{3,1}(0)\big] + \bar{\varepsilon}_{33}\frac{V}{t_p}\big(t_b + t_p\big)L_1 \end{aligned} \tag{17}$$

For each beam we have the current and output voltage of the two components:

$$I = I_2 + I_3 = \frac{V}{Z_L} \tag{18}$$

$$I = -\dot{Q} \tag{19}$$

The output electrical power is decided by the following equation:

$$P = \frac{1}{2}(\bar{I}\bar{V}^* + \bar{I}^*\bar{V}) \tag{20}$$

This simplified impedance relation is often used for evaluating power efficiency of piezoelectric beams [30].

Here we use the common solution for differential equations, where we define general solutions and plug them into the boundary conditions of the system. Therefore, first here we define the boundary conditions as follows:

Displacement B.C. at x_1=0	$u_{211}(0,t) = Asin\theta\exp(i\omega t)$	
	$u_{311}(0,t) = Acos\theta\exp(i\omega t)$	
	$u_{212}(0,t) = Acos\theta\exp(i\omega t)$	
	$u_{312}(0,t) = Asin\theta\exp(i\omega t)$	
Velocity B.C. at x_1=0	$u_{211,1}(0,t) = 0$	
	$u_{311,1}(0,t) = 0$	
	$u_{212}(0,t) = 0$	
	$u_{312}(0,t) = 0$	
Displacement B.C. at L_1	$u_{211}(L_1,t) = u_{221}(L_1,t)$	
	$u_{311}(L_1,t) = u_{321}(L_1,t)$	
	$u_{212}(L_1,t) = u_{222}(L_1,t)$	
	$u_{312}(L_1,t) = u_{322}(L_1,t)$	
Velocity B.C. at L_1	$u_{211,1}(L_1,t) = u_{221,1}(L_1,t)$	
	$u_{311,1}(L_1,t) = u_{321,1}(L_1,t)$	(21)
	$u_{212,1}(L_1,t) = u_{222,1}(L_1,t)$	
	$u_{312,1}(L_1,t) = u_{322,1}(L_1,t)$	
Momentum B.C at L_1	$M_{211}(L_1,t) = M_{221}(L_1,t)$	
	Which equals: $-D_{211}.u_{211,11} = -D_{221}.u_{221,11}$	
	$M_{311}(L_1,t) = M_{321}(L_1,t)$	
	$M_{212}(L_1,t) = M_{222}(L_1,t)$	
	$M_{312}(L_1,t) = M_{322}(L_1,t)$	
Shear B.C. at L_1	$N_{211}(L_1,t) = N_{221}(L_1,t)$	
	Which equals: $-D_{211}.u_{211,111} = -D_{221}.u_{221,111}$	
	$N_{311}(L_1,t) = N_{321}(L_1,t)$	
	$N_{212}(L_1,t) = N_{222}(L_1,t)$	
	$N_{312}(L_1,t) = N_{322}(L_1,t)$	
Momentum B.C. at $L_1 + L_2$	$M_{221}(L_1 + L_2,t) = 0$	

$$M_{321}(L_1 + L_2, t) = 0$$
$$M_{222}(L_1 + L_2, t) = 0$$
$$M_{322}(L_1 + L_2, t) = 0$$

Shear at L_2

$$-N_{221}(L_2, t) = m_0 \ddot{u}_{221}(L_2, t)$$
$$-N_{321}(L_2, t) = m_0 \ddot{u}_{321}(L_2, t)$$
$$-N_{222}(L_2, t) = m_0 \ddot{u}_{222}(L_2, t)$$
$$-N_{322}(L_2, t) = m_0 \ddot{u}_{322}(L_2, t)$$

We also use the complex notation for time-harmonic motion:

$$\{u_{211}, u_{311}, u_{221}, u_{321}, u_{212}, u_{312}, u_{222}, u_{322}, V, Q, I\} = Re\{\{f_1, f_2, f_3, f_4, f_5, f_5, f_6, f_7, f_8, \bar{V}, \bar{Q}, \bar{I}\} \exp(i\omega t)\} \quad (22)$$

The general solution to (15) for the 1st and 2nd beams are:

$$\begin{aligned}
f1 &= B_1 \sin(\alpha x_1) + B_2 \cos(\alpha x_1) + B_3 \sinh(\alpha x_1) + B_4 \cosh(\alpha x_1) \\
f2 &:= B_5 sin(\beta x_1) + B_6 cos(\beta x_1) + B_7 sinh(\beta x_1) + B_8 cosh(\beta x_1) \\
f3 &:= B_9 sin(\gamma x_1) + B_{10} cos(\gamma x_1) + B_{11} sinh(\gamma x_1) + B_{12} cosh(\gamma x_1) \\
f4 &:= B_{13} sin(\delta x_1) + B_{14} cos(\delta x_1) + B_{15} sinh(\delta x_1) + B_{16} cosh(\delta x_1) \\
f5 &:= B_{17} sin(\epsilon x_1) + B_{18} cos(\epsilon x_1) + B_{19} sinh(\epsilon x_1) + B_{20} cosh(\epsilon x_1) \\
f6 &:= B_{21} sin(\zeta x_1) + B_{22} cos(\zeta x_1) + B_{23} sinh(\zeta x_1) + B_{24} cosh(\zeta x_1) \\
f7 &:= B_{25} sin(\eta x_1) + B_{26} cos(\eta x_1) + B_{27} sinh(\eta x_1) + B_{28} cosh(\eta x_1) \\
f8 &:= B_{29} sin(\kappa x_1) + B_{30} cos(\kappa x_1) + B_{31} sinh(\kappa x_1) + B_{32} cosh(\kappa x_1)
\end{aligned} \quad (23)$$

Therefore, we have 8 general solution equations which will be 9 when the current equation is added. Also, there would be 33 undetermined constants.

In (23):

$$\alpha = \left(\frac{m_1\omega^2}{D_1}\right)^{\frac{1}{4}}, \beta = \left(\frac{m_2\omega^2}{D_2}\right)^{\frac{1}{4}}, \gamma = \left(\frac{m_3\omega^2}{D_3}\right)^{\frac{1}{4}}, \delta = \left(\frac{m_4\omega^2}{D_4}\right)^{\frac{1}{4}}, \epsilon = \left(\frac{m_5\omega^2}{D_5}\right)^{\frac{1}{4}},$$
$$\zeta = \left(\frac{m_6\omega^2}{D_6}\right)^{\frac{1}{4}}, \eta = \left(\frac{m_7\omega^2}{D_7}\right)^{\frac{1}{4}}, \kappa = \left(\frac{m_8\omega^2}{D_8}\right)^{\frac{1}{4}} \quad (24)$$

By substituting (23) in boundary conditions (21) we get the explicit forms of equations for B_1-B_{32}. The equations are written for each beam respectively:

$$
\begin{aligned}
B_2 + B_4 &= Asin(\theta)\\
B_6 + B_8 &= Acos(\theta)\\
B_1\alpha + B_3\alpha &= 0\\
B_5\beta + B_7\beta &= 0\\
B_1 sin(\alpha L_1) + B_2 cos(\alpha L_1) + B_3 sinh(\alpha L_1) + B_4 cosh(\alpha L_1)&\\
= B_9 sin(\gamma L_1) + B_{10} cos(\gamma L_1) + B_{11} sinh(\gamma L_1) + B_{12} cosh(\gamma L_1)&\\
B_5 sin(\beta L1) + B6 * cos(\beta L_1) + B_7 sinh(\beta L_1) + B_8 cosh(\beta L_1)&\\
= B_{13} sin(\delta L_1) + B_{14} cos(\delta L_1) + B_{15} sinh(\delta L_1) + B_{16} cosh(\delta L_1)&\\
B_1 cos(\alpha L_1)\alpha - B_2 sin(\alpha L_1)\alpha + B_3 cosh(\alpha L_1)\alpha + B_4 sinh(\alpha L_1)\alpha&\\
= B_9 cos(\gamma L_1)\gamma - B_{10} sin(\gamma L_1)\gamma + B_{11} cosh(\gamma L_1)\gamma + B_{12} sinh(\gamma L_1)\gamma&\\
B_5 cos(\beta L_1)\beta - B_6 sin(\beta L_1)\beta + B_7 cosh(\beta L_1)\beta + B_8 sinh(\beta L_1)\beta&\\
= B_{13} cos(\delta L_1)\delta - B_{14} sin(\delta L_1)\delta + B_{15} cosh(\delta L_1)\delta + B_{16} sinh(\delta L_1)\delta&\\
-D_{211}(-B_1 sin(\alpha L_1)\alpha^2 - B_2 cos(\alpha L_1)\alpha^2 + B_3 sinh(\alpha L_1)\alpha^2 + B_4 cosh(\alpha L_1)\alpha^2)&\\
+ D_{31} E_l G_{211}/s_{11}&\\
= -D_{1221}(-B_9 sin(\gamma L_1)\gamma^2 - B_{10} cos(\gamma L_1)\gamma^2 + B_{11} sinh(\gamma L_1)\gamma^2&\\
+ B_{12} cosh(\gamma L_1)\gamma^2)&\\
-D_{311}(-B_5 sin(\beta L_1)\beta^2 - B_6 cos(\beta L_1)\beta^2 + B_7 sinh(\beta L_1)\beta^2 + B_8 cosh(\beta L_1)\beta^2)&\\
+ D_{31} E_l G_{311}/s_{11}&\\
= -D_{321}(-B_{13} sin(\delta L_1)\delta^2 - B_{14} cos(\delta L_1)\delta^2 + B_{15} sinh(\delta L_1)\delta^2&\\
+ B_{16} cosh(\delta L_1)\delta^2)&\\
-D_{211}(-B_1 cos(\alpha L_1)\alpha^3 + B_2 sin(\alpha L_1)\alpha^3 + B_3 cosh(\alpha L_1)\alpha^3 + B_4 sinh(\alpha L_1)\alpha^3)&\\
= -D_{221}(-B_9 cos(\gamma L_1)\gamma^3 + B_{10} sin(\gamma L_1)\gamma^3 + B_{11} cosh(\gamma L_1)\gamma^3&\\
+ B_{12} sinh(\gamma L_1)\gamma^3)&\\
-D_{311}(-B_5 cos(\beta L_1)\beta^3 + B_6 sin(\beta L_1)\beta^3 + B_7 cosh(\beta L_1)\beta^3 + B_8 sinh(\beta L_1)\beta^3)&\\
= -D_{321}(-B_{13} cos(\delta L_1)\delta^3 + B_{14} sin(\delta L_1)\delta^3 + B_{15} cosh(\delta L_1)\delta^3&\\
+ B_{16} sinh(\delta L_1)\delta^3)&\\
-D_{221}(-B_9 sin(\gamma(L_1 + L_2))\gamma^2 - B_{10} cos(\gamma(L_1 + L_2))\gamma^2 + B_{11} sinh(\gamma(L_1 + L_2))\gamma^2&\\
+ B_{12} cosh(\gamma(L_1 + L_2))\gamma^2) = 0&\\
-D_{321}(-B_{13} sin(\delta(L_1 + L_2))\delta^2 - B_{14} cos(\delta(L_1 + L_2))\delta^2 + B_{15} sinh(\delta(L_1 + L_2))\delta^2&\\
+ B_{16} cosh(\delta(L_1 + L_2))\delta^2) = 0&\\
-D_{221}(-B_9 cos(\gamma L_2)\gamma^3 + B_{10} sin(\gamma L_2)\gamma^3 + B_{11} cosh(\gamma L_2)\gamma^3 + B_{12} sinh(\gamma L_2)\gamma^3)&\\
= m_0\omega^2(B_9 sin(\gamma L_2) + B_{10} cos(\gamma L_2) + B_{11} sinh(\gamma L_2) + B_{12} cosh(\gamma L_2))&\\
-D_{321}(-B_{13} cos(\delta L_2)\delta^3 + B_{14} sin(\delta L_2)\delta^3 + B_{15} cosh(\delta L_2)\delta^3 + B_{16} sinh(\delta L_2)\delta^3)&\\
= m_0\omega^2(B_{13} sin(\delta L_2) + B_{14} cos(\delta L_2) + B_{15} sinh(\delta L_2) + B_{16} cosh(\delta L_2))&\\
B_{18} + B_{20} &= A.cos(\theta)\\
B_{22} + B_{24} &= A.sin(\theta)\\
B_{17}\epsilon + B_{19}\epsilon &= 0\\
B_{21}\zeta + B_{23}\zeta &= 0
\end{aligned}
\tag{25}
$$

$$B_{17}sin(\epsilon L_1) + B_{18}cos(\epsilon L_1) + B_{19}sinh(\epsilon L_1) + B_{20}cosh(\epsilon L_1) = B_{25}sin(\eta L_1) + B_{26}cos(\eta L_1) + B_{27}sinh(\eta L_1) + B_{28}cosh(\eta L_1)$$

$$B_{21}sin(\zeta L_1) + B_{22}cos(\zeta L_1) + B_{23}sinh(\zeta L_1) + B_{24}cosh(\zeta L_1) = B_{29}sin(\kappa L_1) + B_{30}cos(\kappa L_1) + B_{31}sinh(\kappa L_1) + B_{32}cosh(\kappa L_1)$$

$$B_{17}cos(\epsilon L_1)\epsilon - B_{18}sin(\epsilon L_1)\epsilon + B_{19}cosh(\epsilon L_1)\epsilon + B_{20}sinh(\epsilon L_1)\epsilon = B_{25}cos(\eta L_1)\eta - B_{26}sin(\eta L_1)\eta + B_{27}cosh(\eta L_1)\eta + B_{28}sinh(\eta L_1)\eta$$

$$B_{21}cos(\zeta L_1)\zeta - B_{22}sin(\zeta L_1)\zeta + B_{23}cosh(\zeta L_1)\zeta + B_{24}sinh(\zeta L_1)\zeta = B_{29}cos(\kappa L_1)\kappa - B_{30}sin(\kappa L_1)\kappa + B_{31}cosh(\kappa L_1)\kappa + B_{32}sinh(\kappa L_1)\kappa$$

$$-D_{312}(-B_{17}sin(\epsilon L_1)\epsilon^2 - B_{18}cos(\epsilon L_1)\epsilon^2 + B_{19}sinh(\epsilon L_1)\epsilon^2 + B_{20}cosh(\epsilon L_1)\epsilon^2) + d_{31}E_l G_{312}/s_{11} = -D_{322}(-B_{25}sin(\eta L_1)\eta^2 - B_{26}cos(\eta L_1)\eta^2 + B_{27}sinh(\eta L_1)\eta^2 + B_{28}cosh(\eta L_1)\eta^2)$$

$$-D_{212}(-B_{21}sin(\zeta L_1)\zeta^2 - B_{22}cos(\zeta L_1)\zeta^2 + B_{23}sinh(\zeta L_1)\zeta^2 + B_{24}cosh(\zeta L_1)\zeta^2) + d_{31}E_l G_{212}/s_{11} = -D_{222}(-B_{29}sin(\kappa L_1)\kappa^2 - B_{30}cos(\kappa L_1)\kappa^2 + B_{31}sinh(\kappa L_1)\kappa^2 + B_{32}cosh(\kappa L_1)\kappa^2)$$

$$-D312(-B_{17}cos(\epsilon L_1)\epsilon^3 + B_{18}sin(\epsilon L_1)\epsilon^3 + B_{19}cosh(\epsilon L_1)\epsilon^3 + B_{20}sinh(\epsilon L_1)\epsilon^3) = -D_{322}(-B_{25}cos(\eta L_1)\eta^3 + B_{26}sin(\eta L_1)\eta^3 + B_{27}cosh(\eta L_1)\eta^3 + B_{28}sinh(\eta L_1)\eta^3)$$

$$-D_{212}(-B_{21}cos(\zeta L_1)\zeta^3 + B_{22}sin(\zeta L_1)\zeta^3 + B_{23}cosh(\zeta L_1)\zeta^3 + B_{24}sinh(\zeta L_1)\zeta^3) = -D_{222}(-B_{29}cos(\kappa L_1)\kappa^3 + B_{30}sin(\kappa L_1)\kappa^3 + B_{31}cosh(\kappa L_1)\kappa^3 + B_{32}sinh(\kappa L_1)\kappa^3)$$

$$-D_{322}(-B_{25}sin\big(\eta(L_1+L_2)\big)\eta^2 - B_{26}cos\big(\eta(L_1+L_2)\big)\eta^2 + B_{27}sinh\big(\eta(L_1+L_2)\big)\eta^2 + B_{28}cosh\big(\eta(L_1+L_2)\big)\eta^2) = 0$$

$$-D_{222}(-B_{29}sin\big(\kappa(L_1+L_2)\big)\kappa^2 - B_{30}cos\big(\kappa(L_1+L_2)\big)\kappa^2 + B_{31}sinh\big(\kappa(L_1+L_2)\big)\kappa^2 + B_{32}cosh\big(\kappa(L_1+L_2)\big)\kappa^2) = 0$$

$$-D_{322}(-B_{25}cos(\eta L_2)\eta^3 + B_{26}sin(\eta L_2)\eta^3 + B_{27}cosh(\eta L_2)\eta^3 + B_{28}sinh(\eta L_2)\eta^3) = m_0\omega^2(B_{25}sin(\eta L_2) + B_{26}cos(\eta L_2) + B_{27}sinh(\eta L_2) + B_{28}cosh(\eta L_2))$$

$$-D_{222}(-B_{29}cos(\kappa L_2)\kappa^3 + B_{30}sin(\kappa L_2)\kappa^3 + B_{31}cosh(\kappa L_2)\kappa^3 + B_{32}sinh(\kappa L_2)\kappa^3) = m_0\omega^2(B_{29}sin(\kappa L_2) + B_{30}cos(\kappa L_2) + B_{31}sinh(\kappa L_2) + B_{32}cosh(\kappa L_2))$$

For the complex expression of voltage of the first and second beam individually, we have:

$$-i\omega\left\{\frac{bd_{31}}{s_{11}}(t_b+t_p)[B_1\alpha cos\alpha L_1-B_2\alpha sin\alpha L_1+B_3\alpha cosh\alpha L_1+B_4\alpha sinh\alpha L_1-\alpha B_1 - \alpha B_3]+\bar{\varepsilon}_{33}\frac{\bar{V}}{t_p}bL_1\right\} - i\omega\left\{\frac{bd_{31}}{s_{11}}(t_b+t_p)[B_5\beta cos\beta L_1-B_6\beta sin\beta L_1+B_8\beta cosh\beta L_1 + B_9\beta sinh\beta L_1-\beta B_5-\beta B_7]+\bar{\varepsilon}_{33}\frac{\bar{V}}{t_p}(t_b+t_p)L_1\right\}=\frac{\bar{V}}{Z_L} \quad (26)$$

$$-i\omega\left\{\frac{cd_{31}}{s_{11}}(t_b+t_p)[B_{17}\epsilon cos\epsilon L_1-B_{18}\epsilon sin\epsilon L_1+B_{19}\epsilon cosh\epsilon L_1+B_{20}\epsilon sinh\epsilon L_1-\epsilon B_{17} - \epsilon B_{19}]+\bar{\varepsilon}_{33}\frac{\bar{V}}{t_p}cL_1\right\} - i\omega\left\{\frac{cd_{31}}{s_{11}}(t_b+t_p)[B_{21}\zeta cos\zeta L_1-B_{22}\zeta sin\zeta L_1+B_{23}\zeta cosh\zeta L_1 + B_{24}\zeta sinh\zeta L_1-\zeta B_{21}-\zeta B_{23}]+\bar{\varepsilon}_{33}\frac{\bar{V}}{t_p}(t_b+t_p)L_1\right\}=\frac{\bar{V}}{Z_L} \quad (27)$$

With the 33 unknowns computed from equations (25-27) by the use of MATLAB (R2013b) the power is then calculated from equation (20).

The calculated analytical results will be showed in Chapter 6 with the same dimensioned used in FEM simulation and Experiment. In the following the experimental approach will be discussed.

3.5. Numerical Quantities and Dimensions

Using the analytical formulation of the mutually perpendicular piezoelectric energy harvesters given in this thesis the problem is solved to show the performance of this approach. And since in each research the dimensions and materials are unique it is better to compare the analytical results with an experiment rather than another reference. Therefore, here we have used PZT-5H polarized ceramics for the piezoelectric sections and an aluminum beam with specifications given in table 3.1 and table 3.2.

Material	Dimension
PZT length	$L_1 = 32\ mm$
PZT thickness	$t_p = 1.48\ mm$
Length of the beam	$L_2 = 25\ cm$
Width of the beam and PZT	$b = 32\ mm$
Thickness of the beam	$t_b = 1.25\ mm$
Tip mass	$m_0 = 10\ grams$

Table 3.1. Beam and PZT dimensions

Material	Property	Value
PZT-5H	$E_p(GPa)$	63
	$\rho\ (kgm^{-3})$	7600
	$s_{11}\ (m^2N^{-1})$	16.8×10^{-12}
	$s_{33}\ (m^2N^{-1})$	20.7×10^{-12}
	$s_{44}\ (m^2N^{-1})$	43.5×10^{-12}
	$s_{12}\ (m^2N^{-1})$	-4.78×10^{-12}
	$s_{13}\ (m^2N^{-1})$	-8.45×10^{-12}
	$d_{31}\ (CN^{-1})$	-175×10^{-12}
	$d_{15}\ (CN^{-1})$	590×10^{-12}
	$d_{33}\ (CN^{-1})$	400×10^{-12}
	$\varepsilon_0(Fm-1)$	$8.854\ \times\ 10^{-12}$
	ε_{11}	$1900\varepsilon_0$
	ε_{33}	$1900\varepsilon_0$
Aluminum	$E_b\ (GPa)$	70
	$\rho\ (kgm^{-3})$	2700

Table 3.2. Piezoelectric and Aluminum Material Properties

The beam and PZT has similar width and we have a tip mass of $m_0 = 10\ grams$

In numerical calculations, we used $s_{11}(1 - iQ^{-1})$ in place of real elastic constant s_{11} since the damping of PZT is included in modeling by using complex values for elastic constant. Q is the quality factor which is assumed to be 10^2 for PZT [31]. The acceleration amplitude $\omega^2 A = 1.0\ m/s^2$ is also fixed in the calculation. For carefully studying the changes in the bandwidth, we

examined a single beam as well as both beams connected together in series of fixed angles and varying angles from 0 to 180 degree.

In the theory we have also considered two other metals to show the effect of changing the alloys. The original metal is an aluminum and once we have used a stainless steel and another time a copper beam. The effects of which can be seen in Chapter 6. And the table of properties can be seen bellow.

Metal Beam Material	Young's Modulus	Density
Aluminum	70 GPa	2700 Kg/m^3
stainless steel - Grade 301	190 GPa	8000 Kg/m^3
copper	117 GPa	8960 Kg/m^3

Table 3.3. Table of Beam's Material

CHAPTER 4

EXPERIMENTAL APPROACH

4.1. Experiment Setup

To evaluate the analytical method an experiment is also carried out with a similar setup. The setup is consisted of the following elements:

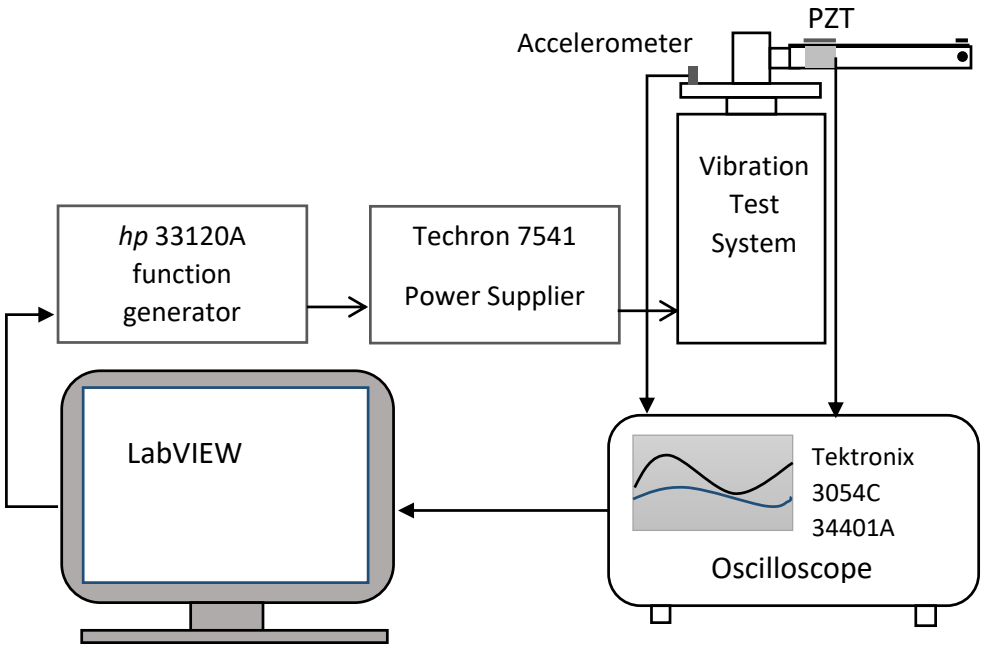

Figure 4.1. Schematic of the experimental setup

In Figure 4.1 we used a PZT material from APC international Ltd (850). The sample has the similar dimension as the analytical solution and the poling direction is along the thickness direction. The setup is once consisted of one aluminum beams attached to a cubic aluminum blocks and then two identical beam in perpendicular directions. The rotating mount is placed on the shaker (VTS Vibration Test System) which vibrate the beams. The shaker is powered by a power supplier (Techron 7541) which itself is fed by a frequency from function wave generator (hp 33120A). An accelerometer (PCB Piezotronics Model 355B04) is also attached to the base of our shaker and a sensitivity of $101.7\ mV/ms^{-2}$ is regarded in our LabVIEW program to keep the

acceleration within $1\,ms^{-2}$ range. The produced voltage is measured by an oscilloscope (Tektronix 3054C) through GPIB cable. The experiment has been monitored by LabVIEW software on a PC connected by signal generator and oscilloscope.

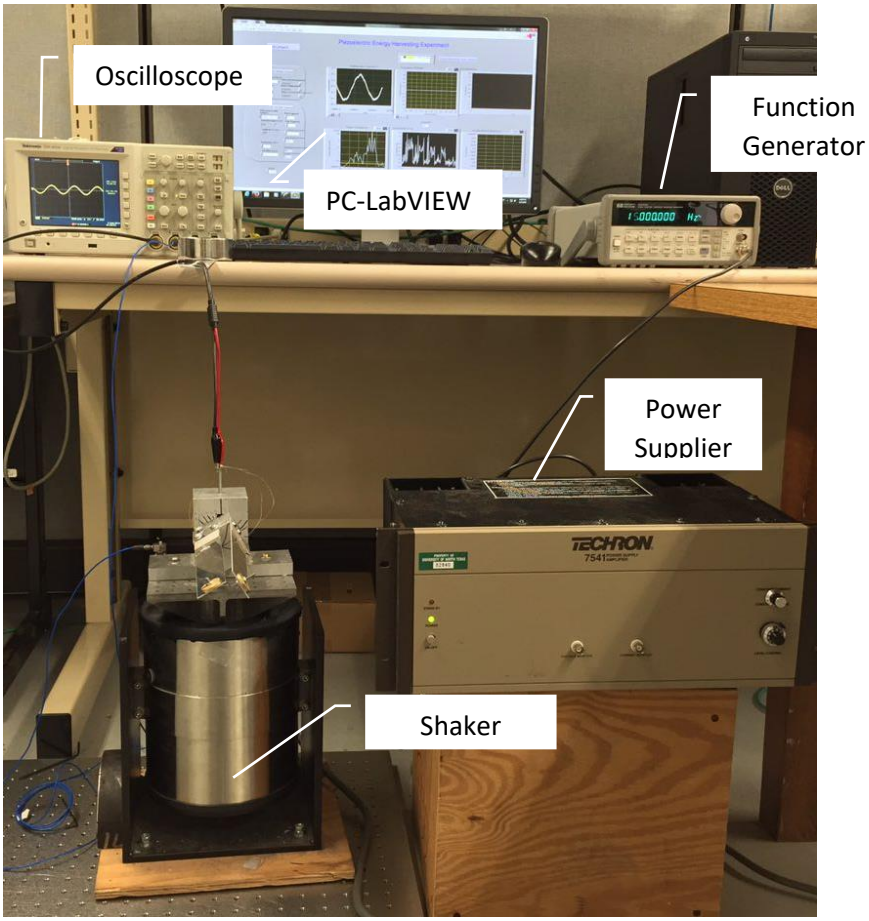

Figure 4.2. A Photograph of experimental configuration

Figure 4.2 is a photograph which shows the experiment setup explained above. They have been set in an order of connection like a loop. Aside from the technical explanation given about for the connections and instruments, in a simpler language it can be said that, the process initiates from LabVIEW. The given frequency sweep goes to Function generator and then to the power supplier which gives the shaker the specified amount of power. The piezoelectric beam is

connected to the shaker which will be discussed in Figure 4.3. The amount of electricity produced from the PZT on the beams will be harvested in oscilloscope and the LabVIEW again.

4.2. Beam and Piezoelectric Configuration

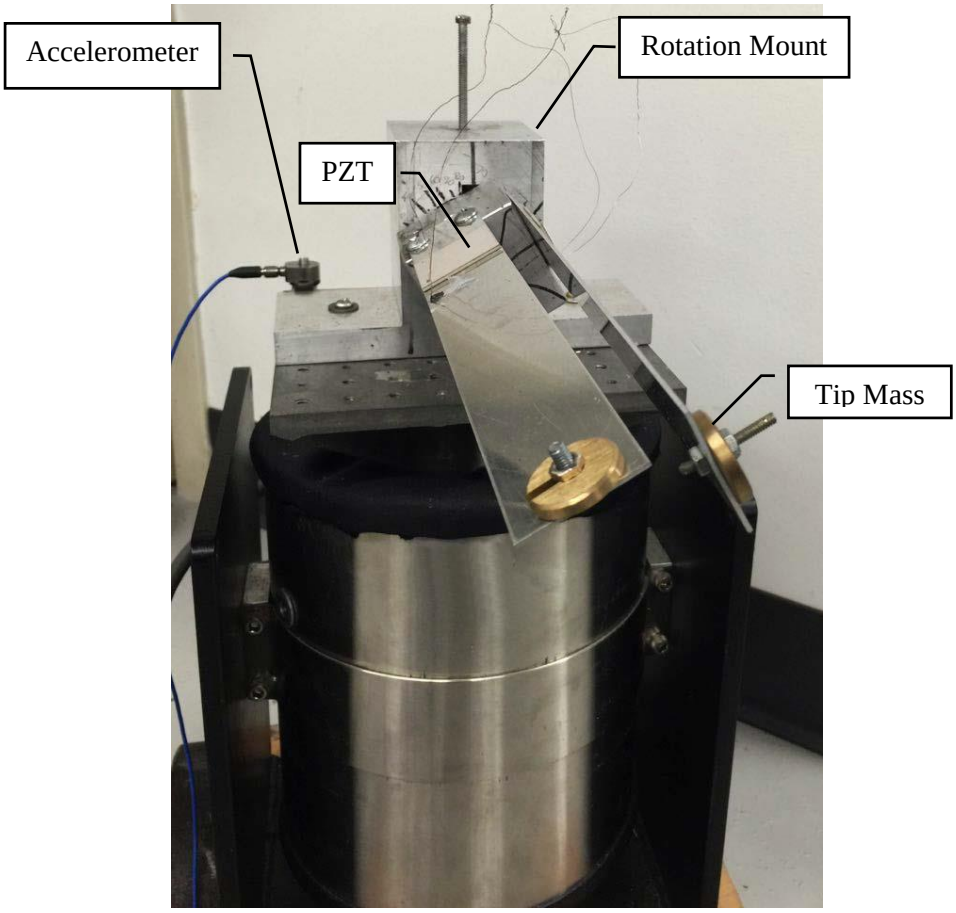

Figure 4.3. A photograph of shaker, beam, PZT, rotation mount and accelerometer

As it can be seen in Figure 4.3 the piezoelectric materials are attached to the beam close to the cantilevered end. There is a brass tip mass on both beams. The accelerometer is connected to the base of the shaker and the beams are connected to a cubic block which itself is lodged inside the rotation block which we have marked with certain rotation angles. It is also clear in this picture that there is enough gap between these two beams.

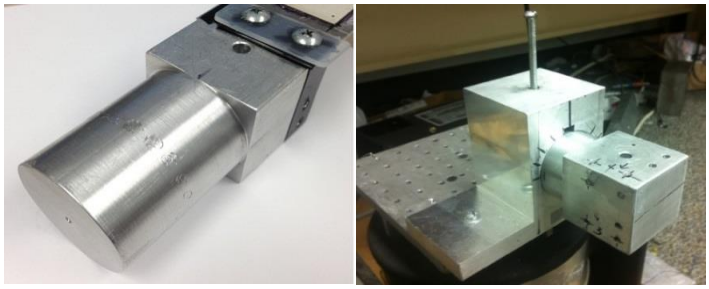

Figure 4.4. The holding gear parts

The holding gear is consisted of two separate blocks, one is the cylinder which rotates and the other is the holder which is fixed on the block. In the following the block diagram used in the LabVIEW will be explained.

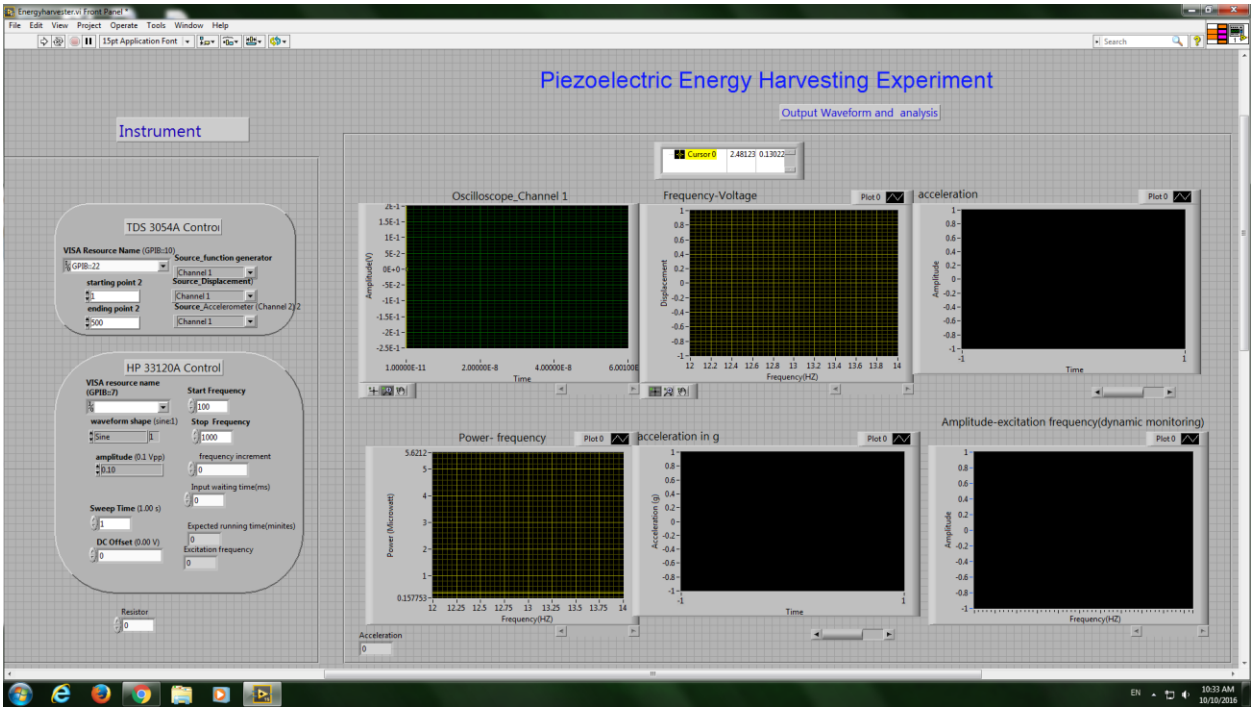

Figure 4.5. Schematic of LabVIEW program

Figure 4.5 shows a screenshot of the block diagrams used in the LabVIEW. In instruments section, the TDS 3054A control block on upper the left shows the input channels, starting and ending points and port selection, which here oscilloscope connects to channel one and

accelerometer connects to channel two. In HP 33120A Control block, the start and stop frequency is set, the step increment which indicates the amount of increment in each sweep is set and also input waiting is being set here which defines the millisecond amount of each frequency pulse to be sent to function generator and then to power supplier. The amplitude of the vibration also will be set here and also waveform shape and the value of impedance for power measurement.

In output waveform analysis section, there is oscilloscope waveform chart, power-frequency-chart, acceleration chart and amplitude-excitation frequency chart. The results of the experiment will be discussed later in chapter 6.

The experiment which is done here has the same parameters as the theory and simulation. However, there are always factors which would elude the analytical methods and there is always a variance between these two methods which is negligible up to a certain amount. The results of experiment will be shown later in this thesis. In the following the procedure used in the FEM simulation will be discussed.

CHAPTER 5

FINITE ELEMENT METHOD SIMULATION

5.1. Simulation Setup

In this thesis a simulation has been done to evaluate the dependency of voltage output to the frequency and even more the dependency of voltage output and frequency value to the rotation angle.

The simulation modeling has been carried out by COMSOL finite element software. The dimensions and properties are the same as in Table 3.1 and 3.2.

Since the purpose of the simulation was to show the faultlessness of the previous approaches and the precision in those methods we avoided using exactly the same configuration and we carried on the simulation for only one single beam with different rotation angles to show the dependency of voltage to rotation angle and also the dependency of rotation on frequency shift.

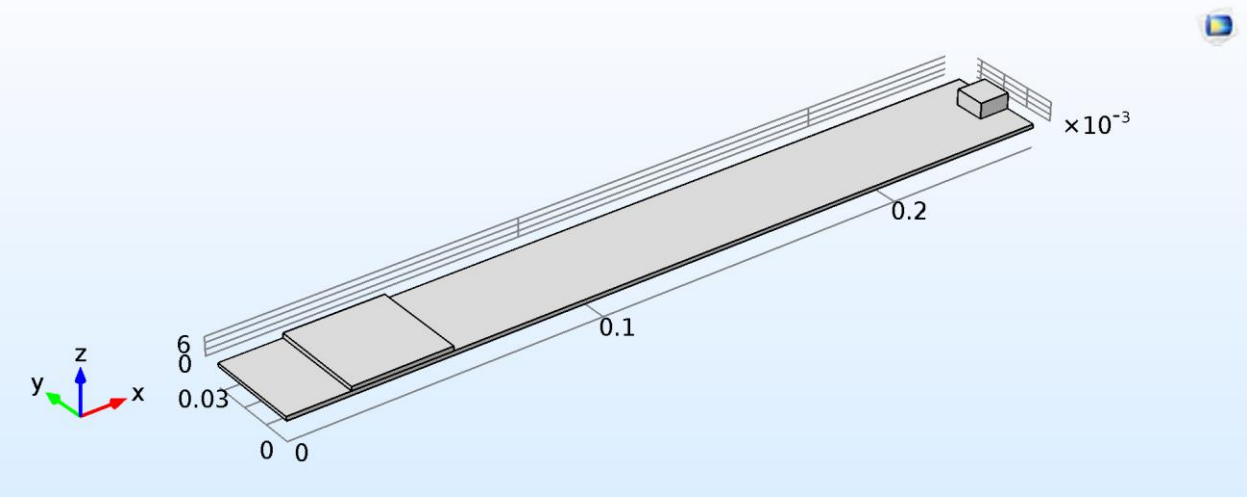

Figure 5.1. COMSOL Beam Model

5.2. Simulation Physics, Study and Meshing

In COMSOL, it is important to know the physics of the simulation. In our case, we used solid mechanics, electrostatics, electrical circuit and piezoelectric material. The solid mechanics will be used for the beam and piezoelectric and electrical physics will be used for electrical circuit.

The simulation have been done under the frequency-domain study. And In the end the amount of voltage has been measured.

After assigning appropriate materials to the model and applying fix-constraint boundary condition to the cantilevered end and also a gravity load to the beam we set the mesh to the whole system. The mesh should be physics-controlled mesh.

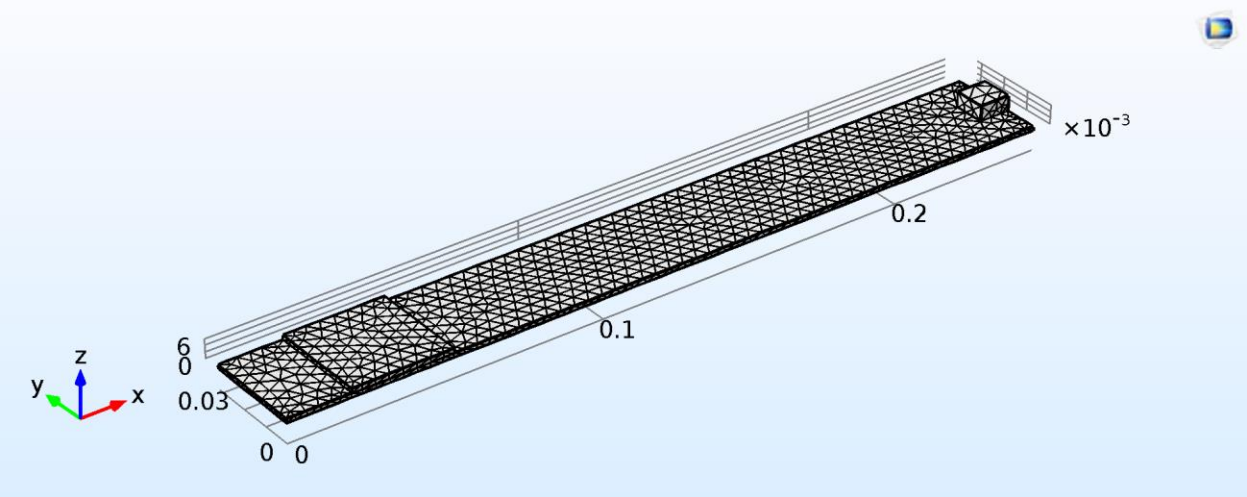

Figure 5.2. Meshing

Figure 5.2 shows the free tetragonal meshing which is actually a physics-controlled meshing. After solving the model for a specific range of frequency we get the desired results. The process has been repeated for several different rotation angles and the results will be shown and discussed in the following chapter.

CHAPTER 6

RESULTS AND DISCUSSIONS

6.1. Analytical Results and Discussion

In this section the results which have been calculated from the numerical evaluation of the theory is presented. The dimensions and properties are mentioned in Table 3.1 and Table 3.2.

6.1.1. Effect of Changing Beam and PZT Length and Thickness on Power vs. Frequency for a Single Beam

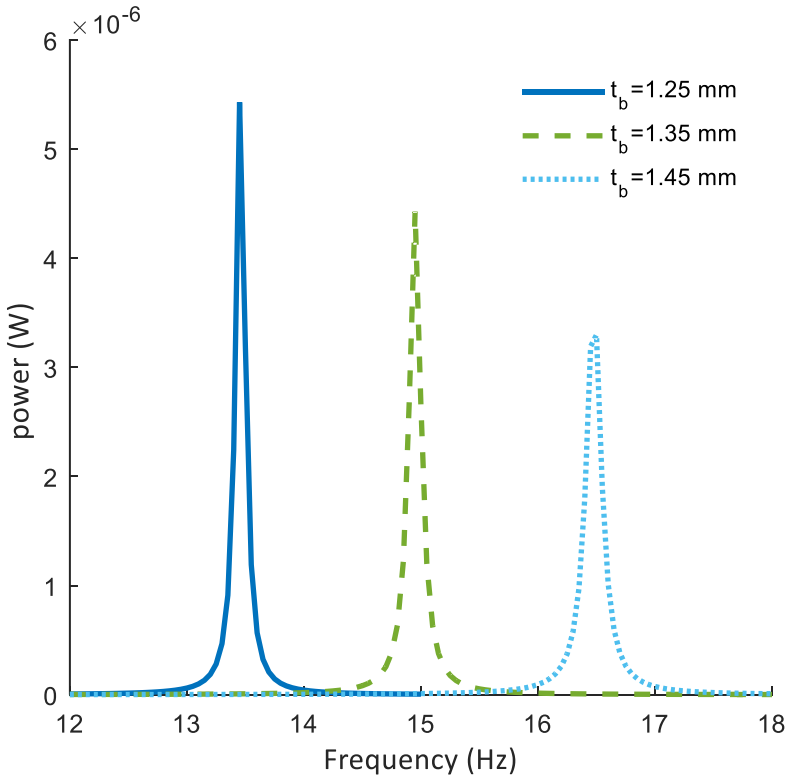

Figure 6.1. Power versus frequency of a single beam at fixed $\mathrm{angle}= 90^{\circ}$, showing the effect of change in beam thickness.

In Figure 6.1, only a single beam at fixed angle of $\theta = 90°$ is studied. As it can be seen, a thicker beam results in lower power. The solid line shows the predefined beam thickness of $t_b =$

$1.25\ mm$, the dashed line is $t_b = 1.11\ mm$, and the dotted line $t_b = 1.49\ mm$. The result here is reasonable because a thicker beam has lower vibration amplitude in its resonant frequency. Furthermore, as it can be seen by increasing the beam thickness, the resonant frequency at which the maximum power happens also increases. The same goes with the change in PZT thickness.

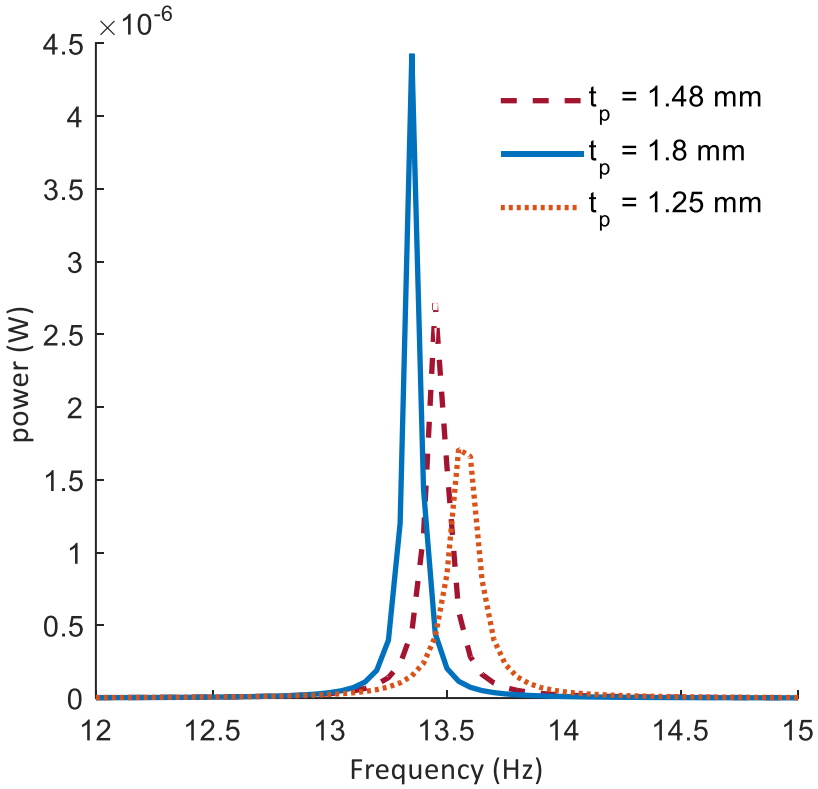

Figure 6.2. Power versus frequency of a single beam at fixed angle =45°, showing the effect of change in PZT thickness.

Figure 6.2 shows the power output versus frequency of a single beam at fixed angle $\theta = 45°$. As it could be seen by decreasing the PZT thickness to $t_p = 1.48\ mm$ (dashed line), the power output decreases and the resonance tend to happen at lower frequency. Also by increasing the PZT thickness to $t_p = 1.8\ mm$ (dotted line), it will have higher peak to the right of the solid graph. The effect of beam length also is of great importance which is depicted in the following graph.

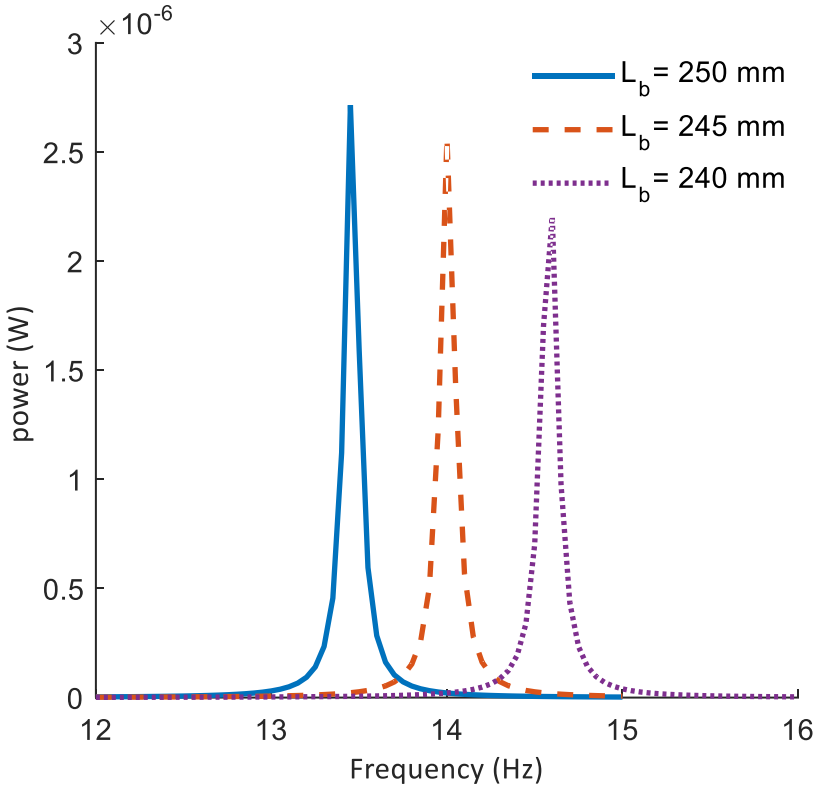

Figure 6.3. Power versus frequency of a single beam at fixed angle =45°, showing the effect of change in beam length.

Figure 6.3 shows the power output versus frequency of a single beam at fixed angle$= 45^{\circ}$. The solid line is for the predefined length of $L_b = 250\ mm$, and the dashed line has a length of $L_b = 245\ mm$. The dotted line is $L_b = 240\ mm$. This is also applicable in case of change in PZT's length as shown in Figure 6.4.

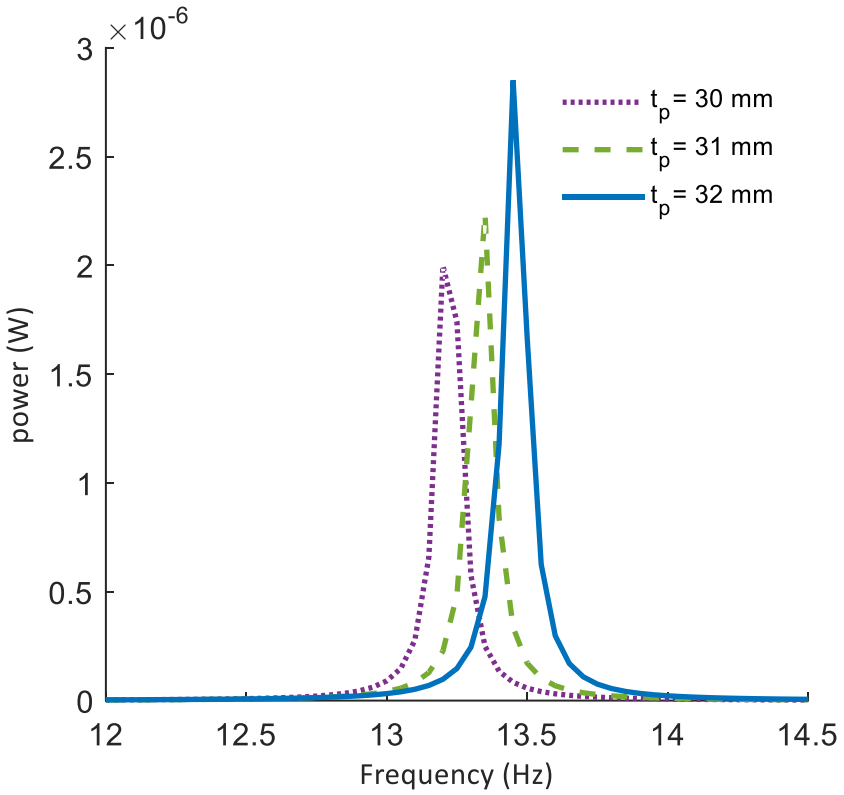

Figure 6.4. Power versus frequency of a single beam at fixed angle =45°, showing the effect of change in PZT length.

Figure 6.4 which also illustrates the power versus frequency of a single beam at fixed angle $\theta = 45^{\circ}$. The dotted line shows the predefined dimension for PZT length which is $L_p = 32\ mm$. The dashed line shows the increase in PZT length to $L_p = 32.5\ mm$ and L_p =33 mm for the solid line. As a result, the power output increases because the PZT area is increased. Hitherto, the power versus frequency is studied only for a fixed angle. In the following paragraphs the effect of the aforementioned changes is going to be examined for varying angles in a single beam.

6.1.2. Effect of Changing Beam and PZT Length and Thickness on Power vs. Angle for a Single Beam

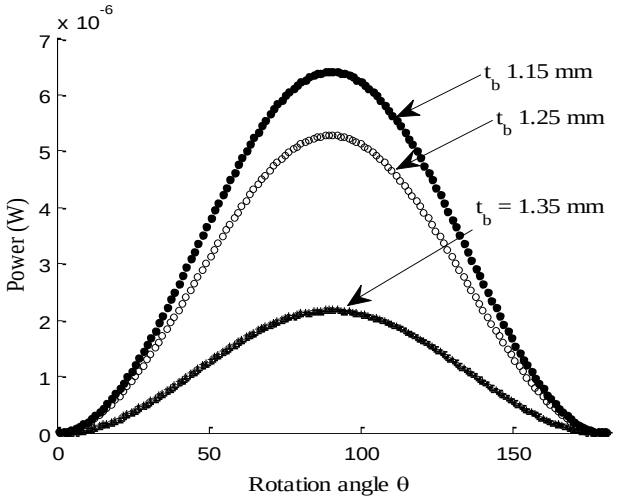

Figure 6.5. Output power versus θ, showing the effect of changing beam thickness.

Figure 6.5 shows the output power versus angle θ from 0 to 180 degrees. For a single beam, the maximum power happens when $\theta = 90$. Also, the power output decreases when the beam thickness is increased. The same thing happens by changing the PZT thickness, however, the power output increases by increasing PZT thickness which is shown in Figure 6.6.

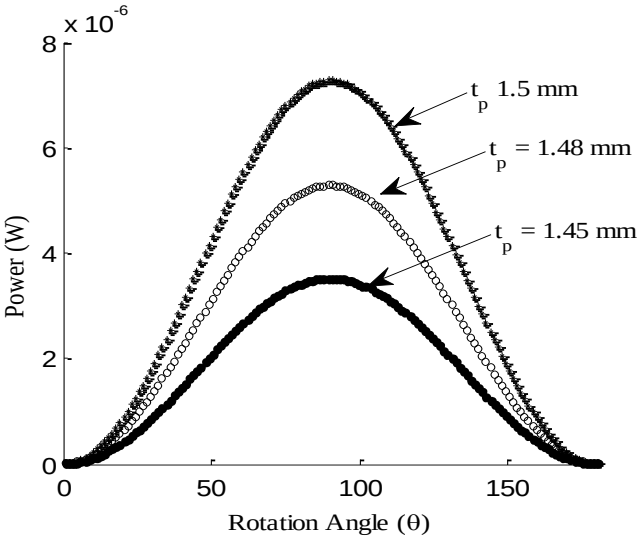

Figure 6.6. Power versus rotation angle, showing the effect of changing PZT thickness.

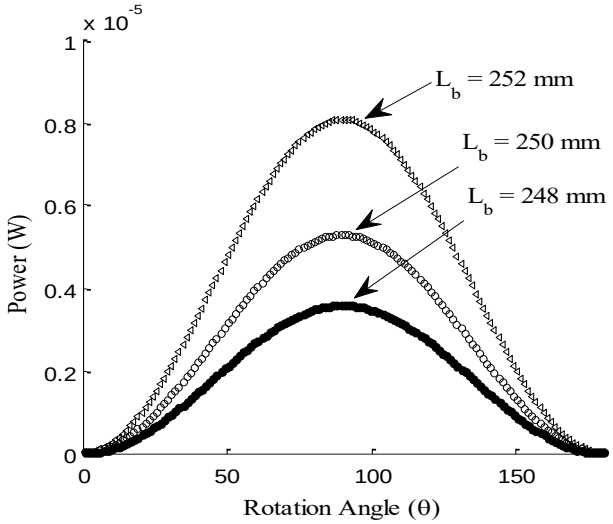

Figure 6.7. Power versus rotation angle, showing the effect of changing Beam Length.

The effect of beam and PZT length is also shown in Figure 6.7 and 6.8. In *Figure 6.7* the power versus angle is shown from 0 to 180 degree for a single beam. The beam length and PZT thickness are more sensitive to dimension changes when investigating the power output (Figure 6.6 and Figure 6.7). It is also sensitive to the changes in the PZT lengths (here from $L_p = 35\ mm$ to $L_p = 32\ mm$ and $L_p = 33\ mm$) which is also depicted in Figure 6.8 Longer PZTs result in greater output.

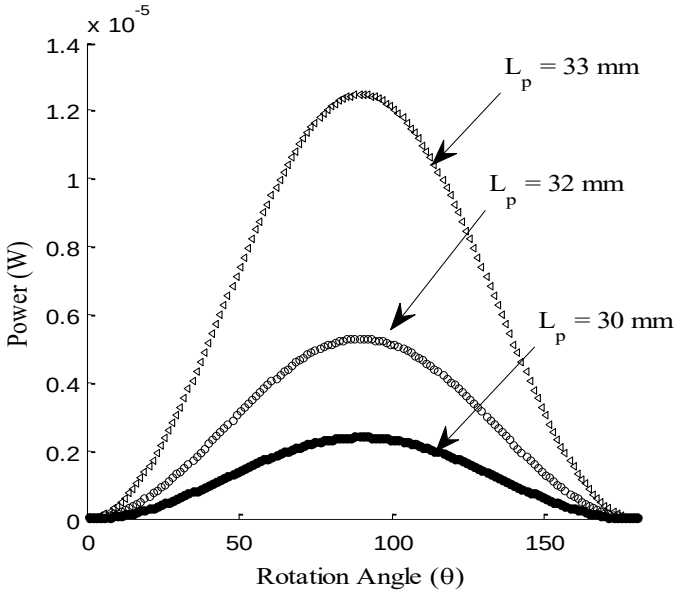

Figure 6.8. Power versus rotation angle, showing the effect of PZT length

6.1.3. Effect of Changing Beam and PZT Length and Thickness on Area vs. Angle Graph for a Single Beam

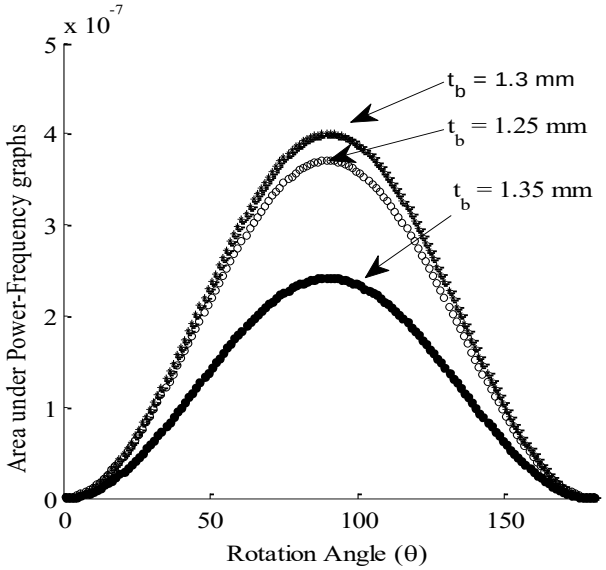

Figure 6.9. Area under the p-ω versus rotation angle for a single beam with changes in beam's thickness

Another criteria for measuring and comparing the harvested energy of these systems is to measure the area under the curve of a power versus frequency for each angle from 0 to 180

degree which directly indicate the bandwidth area and it's a good measure of power. Figure 6.9 and Figure 6.10 show the effect of thickness change on this criteria. In Figure 6.9 it is shown that by increasing beam thickness the value of the $p - \omega$ area decreases. This effect is also applicable for PZT thickness change as shown in Figure 6.10.

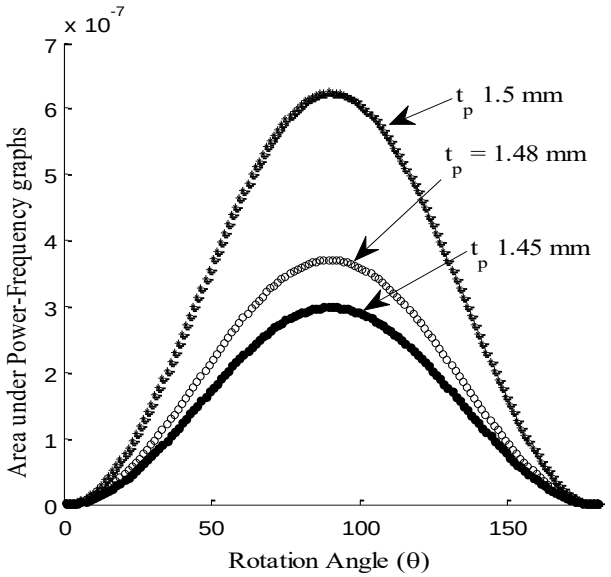

Figure 6.10. Area under the p-ω versus angle for a single beam with changes in PZT's thickness

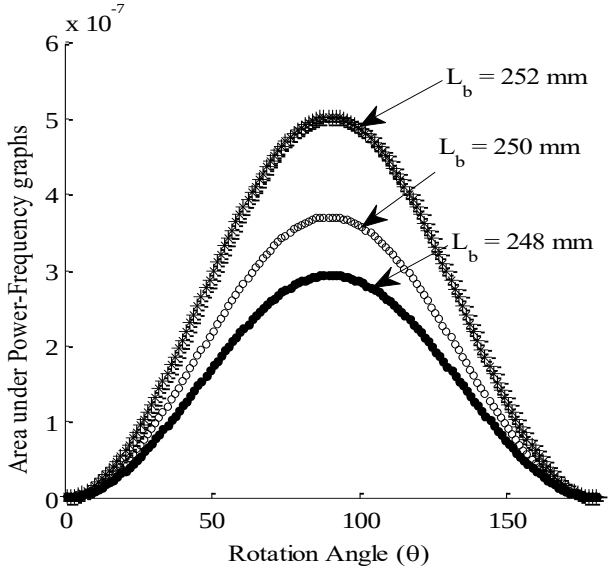

Figure 6.11. Area under the p-ω versus angle for a single beam with changes in beam's Length

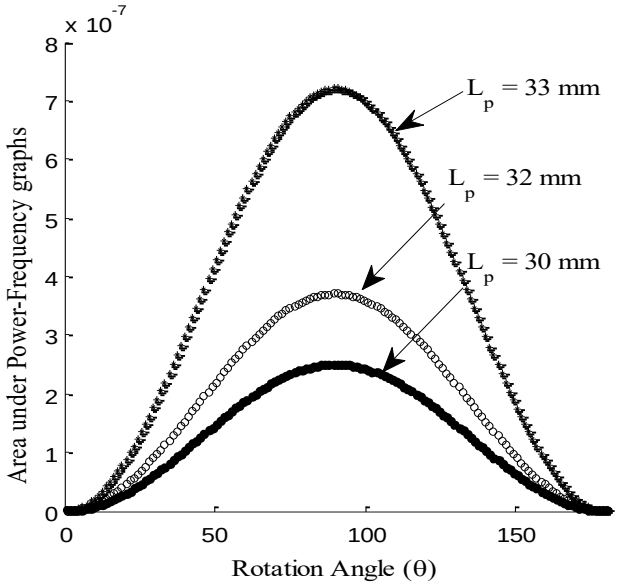

Figure 6.12. Area under the p-ω versus angle for a single beam with changes in PZT's length

Where by increasing the PZT thickness, the $p - \omega$ area increases and vice versa. Figure 6.11 shows the effect of length over the $p - \omega$ area versus angle for a single beam. By decreasing the length of the beam (Momentum arm) the $p - \omega$ area decreases. Inversely if we increase the PZT length, the area under $p - \omega$ curve increases like in Figure 6.12, which shows the area under $p - \omega$ curve versus rotation angles for a single beam. By increasing PZT length more power is produced so the area under the curve increases.

As depicted initially in Figure 3.1 and Figure 4.3, there are two beams in our system which are connected together in series. Therefore, we discuss it more in the following.

6.1.4. Studying the Beam's Material on Power and Frequency

As it can be seen in Figure 6.13 the selection of material for the beam plays an important role. A material which is a little tougher than Aluminum with higher density can lead to more power production at 45 degree. And a material like stainless steel can lead to lower power and a shift of frequency to the right.

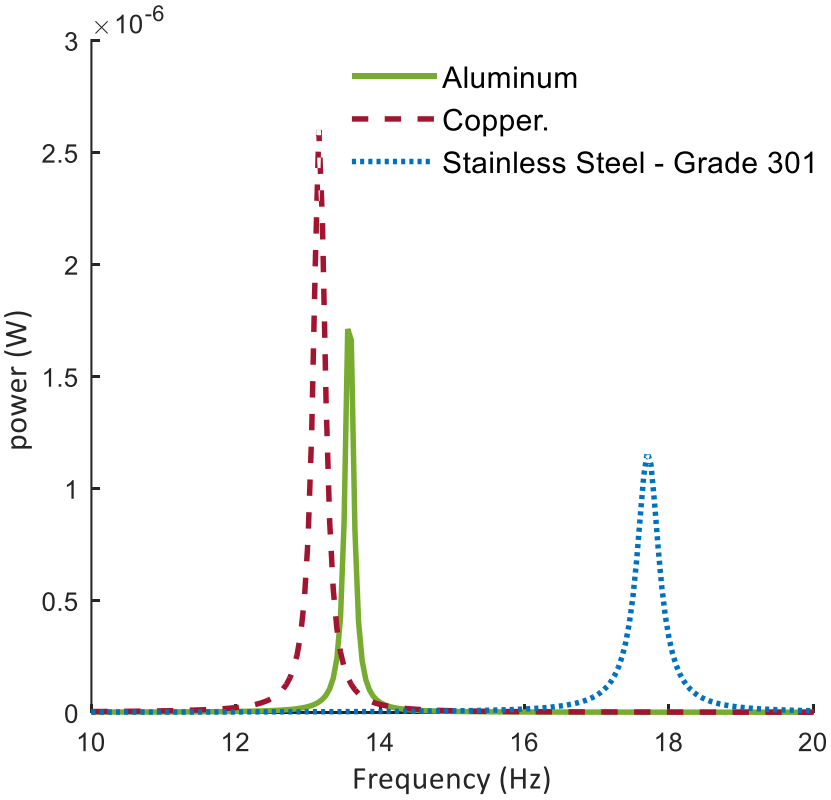

Figure 6.13. Power vs. Frequency for three different materials

6.1.5. Studying the Bandwidth and Power Output of Mutually Perpendicular Beams

The overall calculation of the system is consisted of both beams together. The beams have a fixed angles between them. However, the overall rotation angles would be changed.

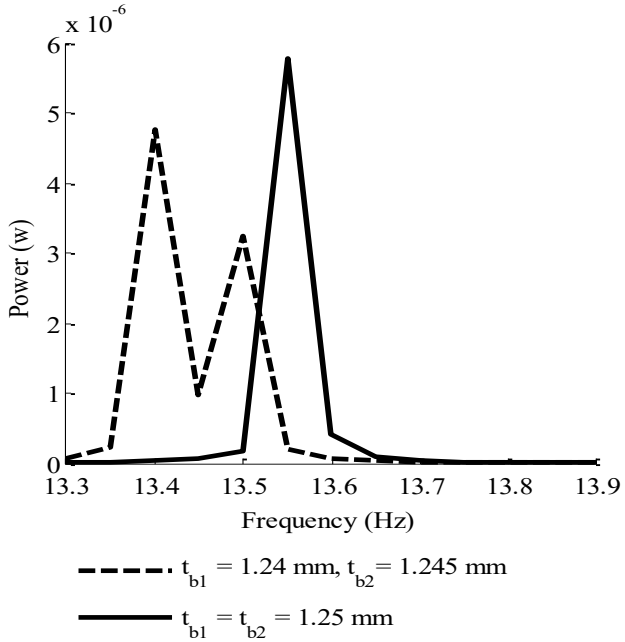

Figure 6.14. Power versus frequency of two perpendicular beams at fixed angle $\theta = 45°$

Figure 6.14 shows the output power P versus the driving frequency ω when the rotation angle is $\theta = 45°$ for the first beam and accordingly $\theta = 135$ for the second beam. The frequency range has been considered the same for both beams. The power output is the result of connecting the piezoelectrics in series, in other words, it is the result of $P = (V_1 + V_2)^2/Z_l$. The solid line happens when both beams have identical configurations of beam, piezoelectric length,

and thickness. In the dashed line case, the 1st beam has a thickness of $t_{b_1} = 1.24\,mm$, and the second beam's thickness is $t_{b_2} = 1.245\,mm$. This slight difference in thicknesses cause each beam to have its two separate narrow peaks, which emerge together and create an increased bandwidth. In other words these two peaks are the result of two separate resonance in x_2 and x_3 directions. The first beam has a higher resonance in x_2 direction than the thicker second beam in x_3 direction. The increased bandwidth could also be achieved with other configuration dissimilarities like PZT thickness difference and length and each has its own effect on the bandwidth.

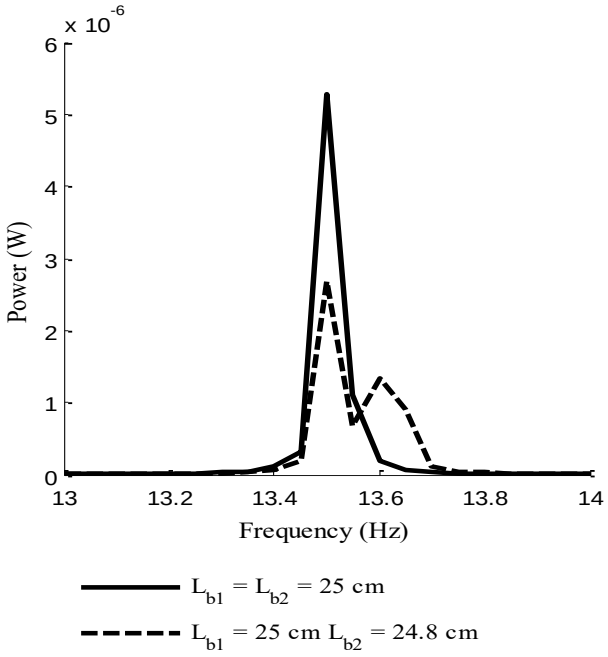

Figure 6.15. Power versus frequency of two perpendicular beams at fixed angle $\theta = 45°$, showing beam length effect on bandwidth

Figure 6.15 shows the output power versus frequency of two perpendicular beams in series connection when the angle is $\theta = 45°$. The solid line shows the resonant frequency of both beams when they have the same length and thickness. The dashed line happens when there is a difference in length of one of the beams. The length of the first beam is being held fixed, and the

first peak belongs to its length of $L_{b_1} = 250\,mm$ and the second peak shows the power of resonant frequency when the length is $L_{b_2} = 248\,mm$ for dashed line. As it can be seen, the wide bandwidth is produced via change in beam length.

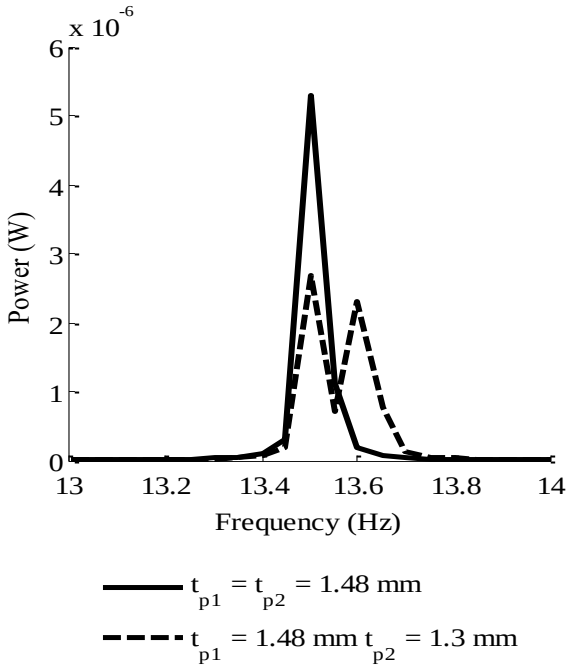

Figure 6.16. Power vs. frequency of two beams at fixed angle $\theta = 45°$ Showing PZT thickness effect on bandwidth.

Figure 6.16 shows the effect of change in beams thicknesses for the first beam. The solid line shows no bandwidth for the fact that both beams have similar PZT thicknesses and the dashed line happens when the second PZT has a thickness $t_{p_2} = 1.3\,mm$. Therefore, it produces a wider bandwidth and furthermore a lower peak due to the lower power output which is in commensurate with the smaller PZT dimensions.

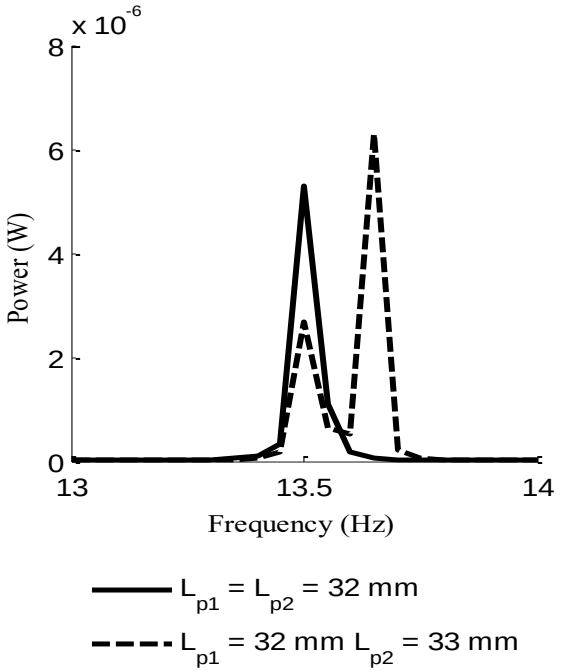

Figure 6.17. Power versus frequency at fixed angle of θ=45°, showing PZT length change effect on bandwidth.

Now we can also see the effect of change in PZT's Length in Figure 6.17 where it explains the effect of increasing PZT length to $L_{p_2} = 33\ mm$ which produce the larger right peak on the dashed line graph and hence produce a larger bandwidth. Therefore, we can say that by carefully adjusting the dimensions of PZT and beam length and thickness, we can achieve a desired bandwidth with these two beams.

6.1.6. Studying the Power Output with Respect to Rotation Angle for Two Beams from 0 to 180 Degree

Now that we discussed about the relation of power versus frequency with different fixed angles, the relation of power versus angles with different frequency will be showed here.

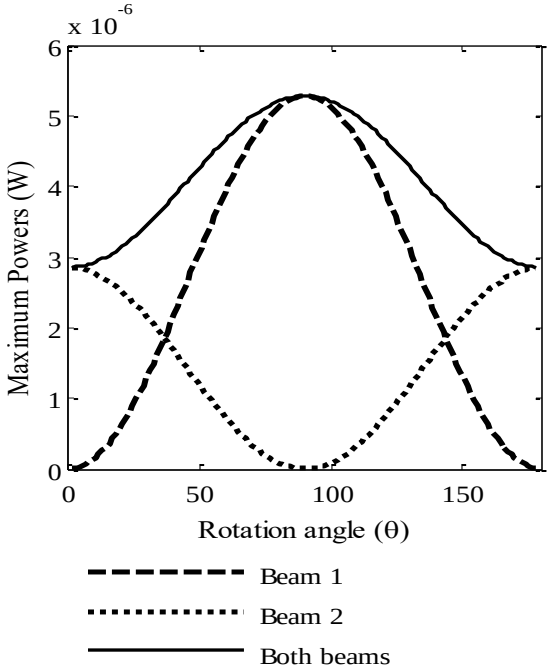

Figure 6.18. Maximum powers versus θ

Figure 6.18 shows the maximum power output of each rotation angles of two mutually perpendicular beams which are attached together in series. The dashed line belongs to the first beam where it has the predefined dimensions and start producing power from vertical position and then reach its culmination point when it is poised in horizontal position $\theta = 90^{\circ}$. The second beam which has a different PZT thickness in this case $t_{p_2} = 1.1\ mm$ will produce less power but has a similar behavior as shown in a dotted line in this figure. When the first beam is in horizontal position the second is in vertical position hence it would have a 90 degree phase lag and when they are added together the addition of the powers would be like the solid line.

6.1.7. Studying the Area Under P-Ω Curve with Respect to Rotation Angle for Two Beams from 0 to 180 Degree

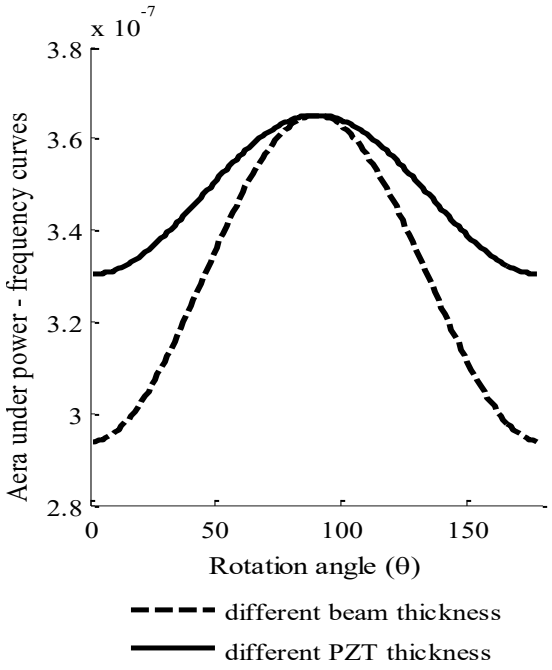

Figure 6.19. Area under p-ω curve versus θ of both beams in series

If we take the area under power versus frequency curve for each angle and plot it, the result will be Figure 6.19 , in which the solid line shows the area values for a system where one beam's thickness is different from the other, in this case $t_{b_2} = 1.24\ mm$. The dashed line shows the area under the curve of a system where their PZT thicknesses are different. Here we tried to show that by adjusting these dimension differences we can both have wider frequency range and also a good measure of power output by regarding the area under the power-frequency curves and maximum powers.

6.1.8. Justification of Frequency Shift Absence in Analytical Results Due to Rotation

As it could be seen here in analytical results, there is no frequency shift related to the rotation angle of the beam. The rotation angle shows only the dependence of power versus frequency and the frequency shift produced in the aforementioned figures results from the change in the dimensional properties of the beam as has been done earlier in [24]. A probable reason for this paucity of frequency shift could be from the effect of pre-stress due to gravity, because the only factor which is missing in the analytical results with comparison to simulation and experiment is the gravity load effect which changes with respect to the rotation angle of the beam and would divide into components.

6.2. Experimental Verification of the Results

As mentioned in chapter 4, an experiment has been carried out to verify the result of the power and frequency for an angular single beam and also a mutually perpendicular beams.

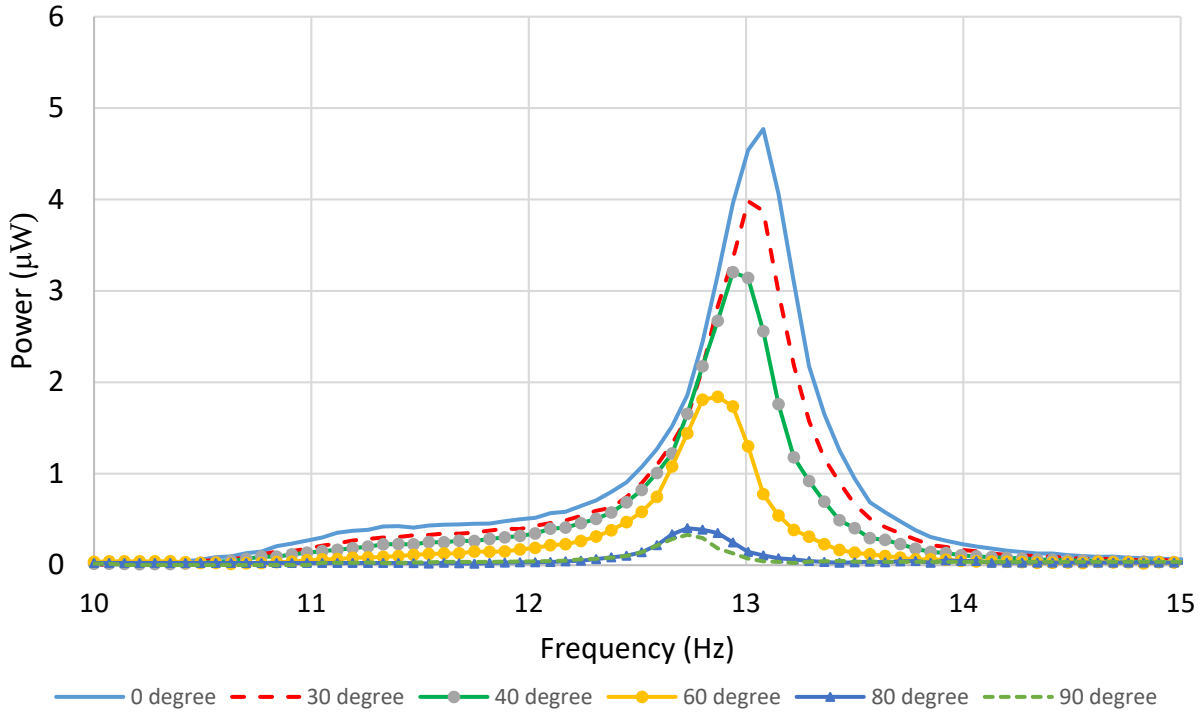

Figure 6.20. Power versus frequency of a single beam with different rotation angles

Figure 6.20 shows the dependence of power to frequency at different angles for only one single piezoelectric cantilever beam. As expected the maximum output voltage belongs to the case where the beam is horizontal (i.e.$\theta = 0$). By changing the beam angle to 20, 40, 60, 80 and 90 degree the output power the power decreases correspondingly. The illustration in Figure 6.21 and the photograph in Figure 6.22 are presented to clarify the position of the single angular beam.

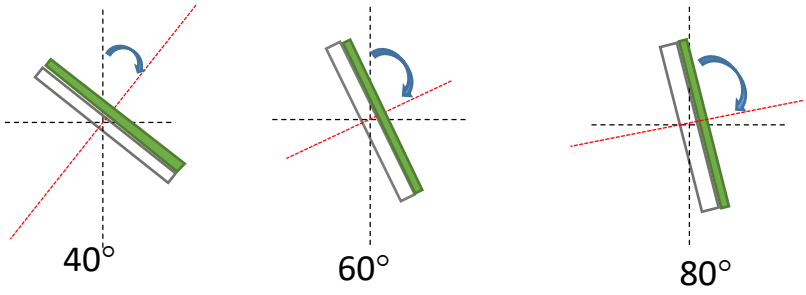

Figure 6.21. Rotation illustration for a single beam

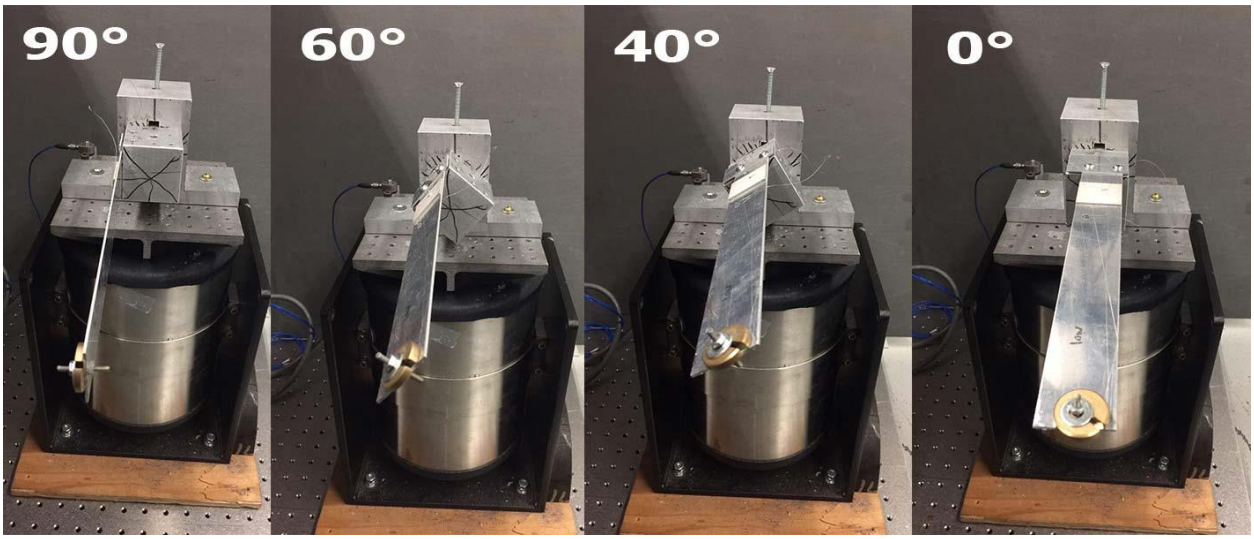

Figure 6.22. Experimental rotation photograph

Furthermore, as it can be seen in Figure 6.20 a frequency shift happens which moves the resonant frequency to the left by giving more angle to the beam. In the following the output power of double beam in two configuration of series and single output is studied.

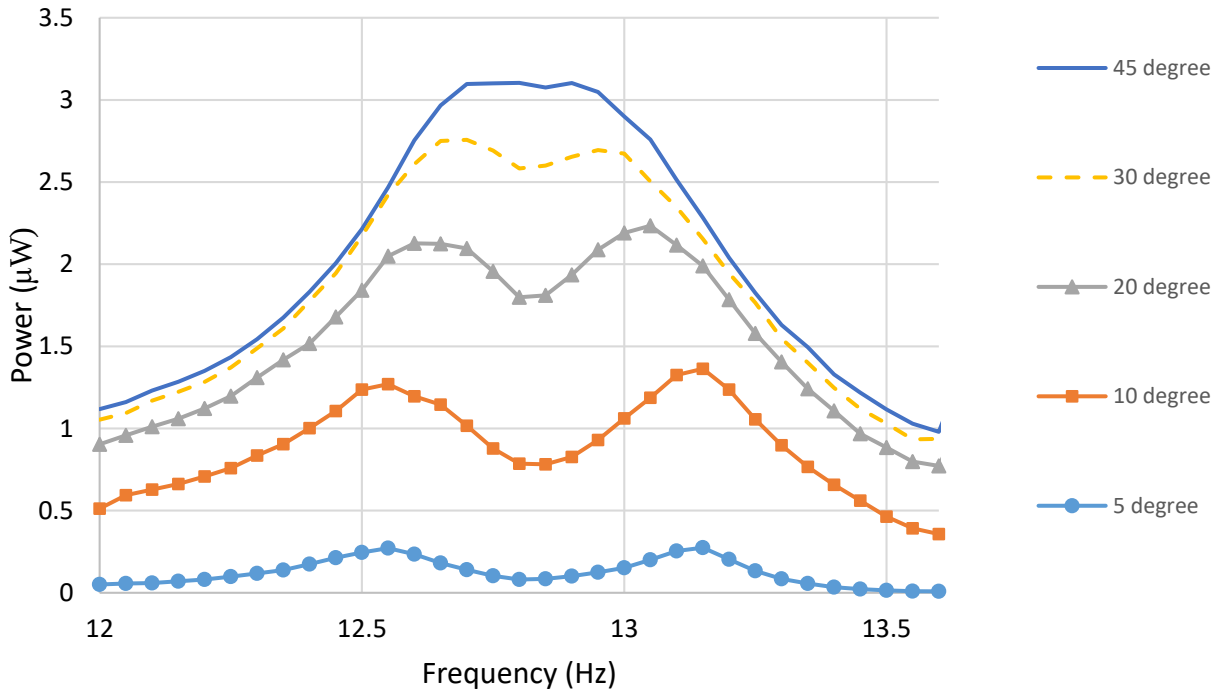

Figure 6.23. Power versus frequency of one perpendicular beam

Figure 6.23 shows the output power to frequency for one mutually perpendicular single piezoelectric cantilever beams. Here each beam has different resonant frequencies and if their output powers are vibrated together they create a wider driving frequency bandwidth. Here we wanted to show the effect of the resonance of one beam on another, therefore, the output only belongs to one beam and the other beam only create another resonance peak to make it wider. Furthermore, the effect of frequency shift on both beams is quite visible in this figure. Here both beams being mutually perpendicular had 45 degrees.

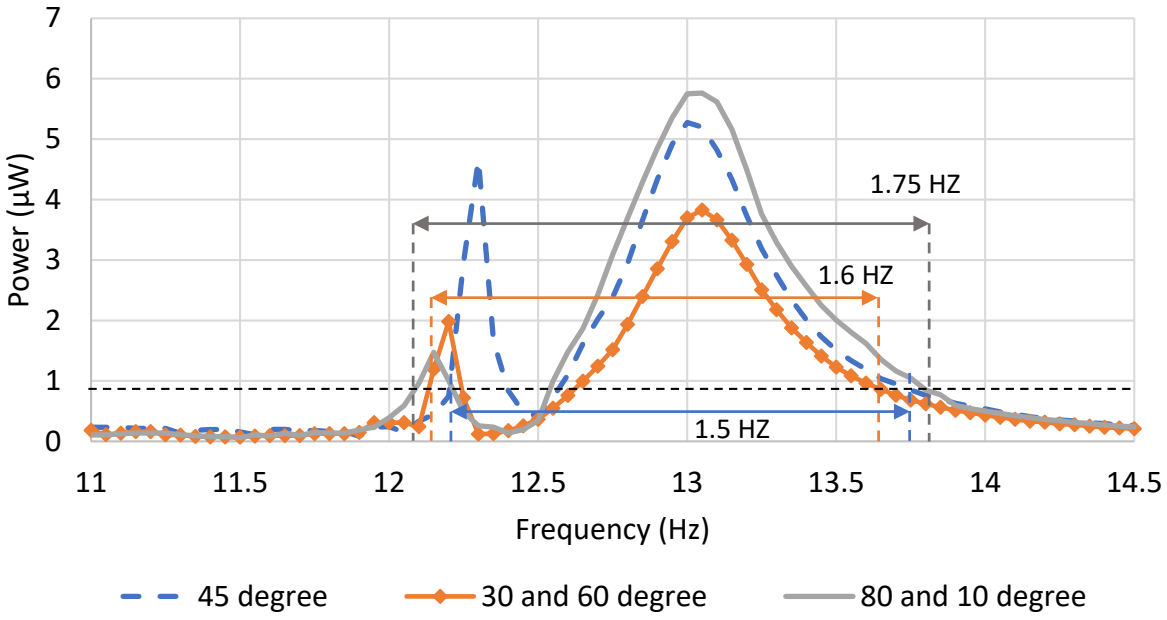

Figure 6.24. Power versus frequency of double perpendicular beams of slightly different length

In contrary to the previous circuit connection, in Figure 6.24 the piezoelectrics are connected in series to each other. That is, like batteries in series the positive end of one PZT is connected to the negative end of the other one and the power is gathered from the positive-negative free ends as it was mentioned in Figure 3.1 for theoretical analysis. When the system is in 45 degree, both beams are at 45 degree and there are two peaks of nearly similar power value. However, because of the difference in the length one beam the peaks are more separate than the similar beams which are also experimented here and noted in Figure 6.28. When the system tilts to 30 degree the other beam is in 60 degree. Hence, it produce more power. Also in the case of 10 and 90 degree, one beam is producing about its maximum power and the other produce its minimum. It is noteworthy to consider the closeness of the values to the theoretical results. Furthermore, as it can be seen in this way a larger bandwidth has been created. Another aspect of this figure is that similar to Figure 6.20 by making one beam 80 degree and one 10 degree the

peaks tends to keep more distance in between and by going to a 45-45 degree for both beams the peaks come closer to each other, which is another verification for experimental results. In the following like single beam to clarify the angular position of double perpendicular beam, an illustration and a photograph has been added.

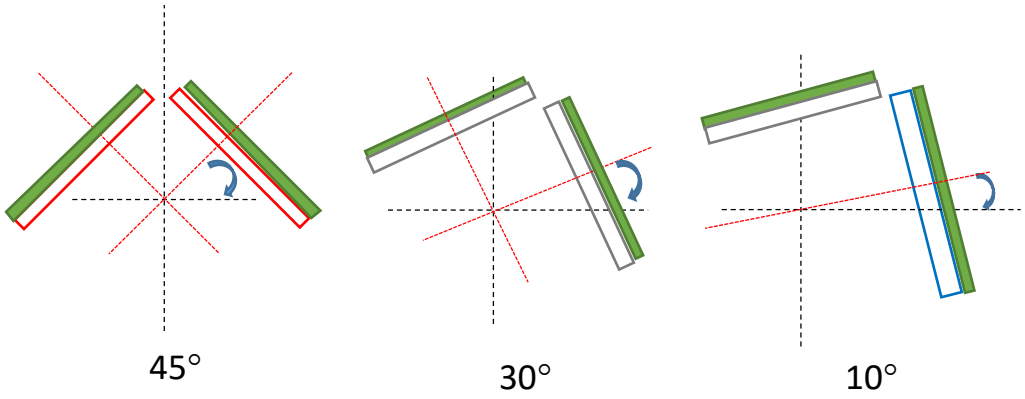

Figure 6.25.IIlustration of double beam angular positions

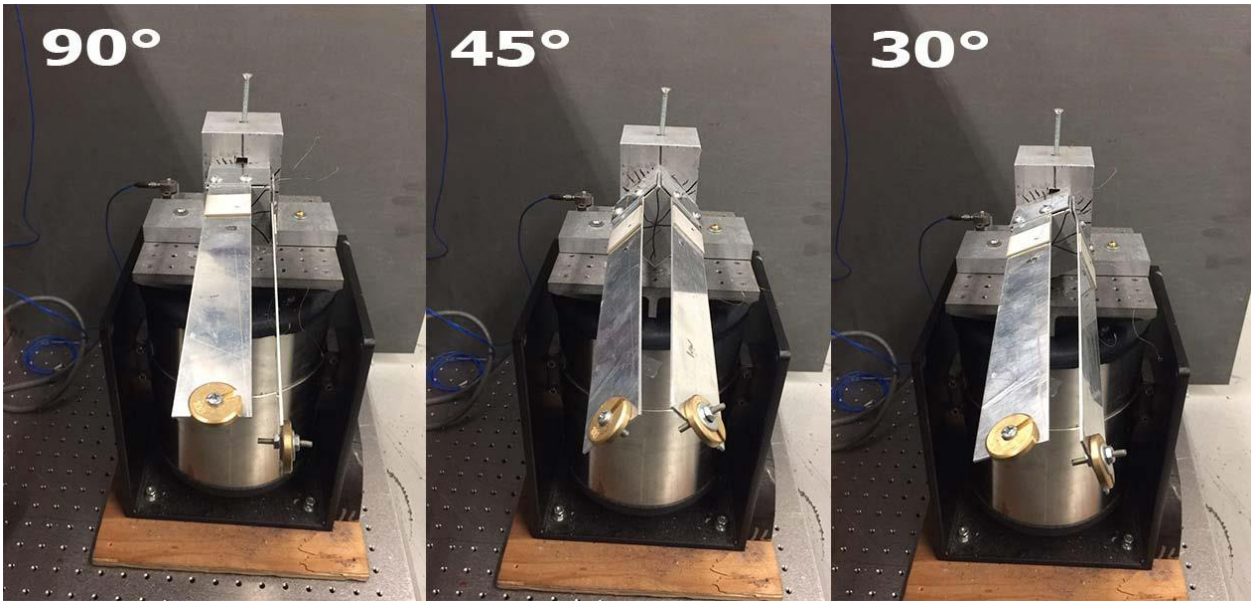

Figure 6.26. Photograph of Double beam

To better observe the effect of rotation on operational frequency bandwidth a separate figure has been plotted bellow. In Figure 6.24 the arrow line is put on $1/\sqrt{2}$ value of the vertical axis as a standard and as it can be seen when the double beams go into a 10 and 80 degree position the bandwidth increase. And as it is shown in Figure 6.27 when beams have more angular difference the bandwidth increase.

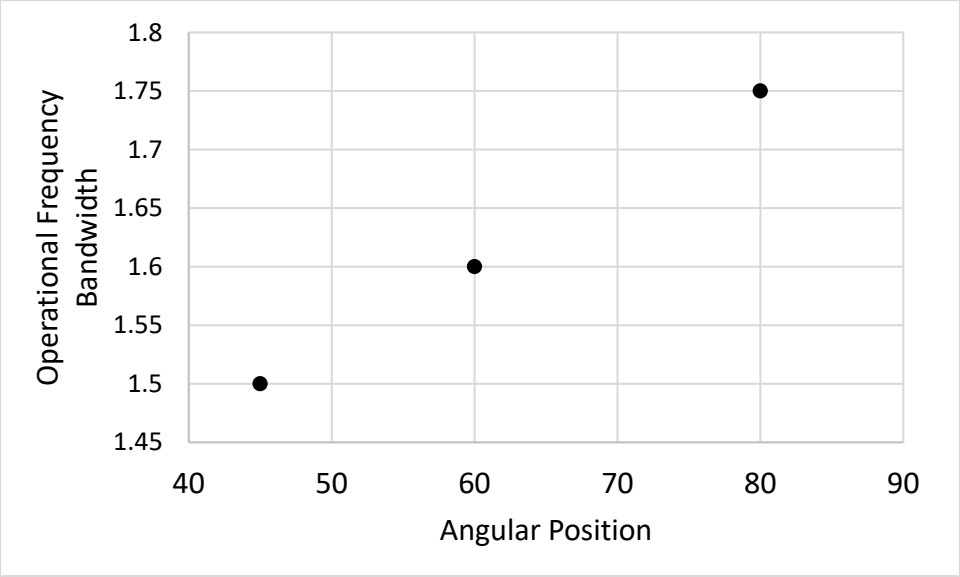

Figure 6.27. Operational frequency bandwidth vs. Angular position of double beam

6.3. Comparison of Experiment and Theory

By comparing the results between the two aforementioned methods we observe that the experimental results corroborate theoretical assumptions and calculations. For instance from Figure 6.1 and Figure 6.20 for a single beam at beam thickness of $t_b = 1.25$ mm which is the same as the experiment's dimensions, the experiment and theory results matches well with each other and they produce a power about 5 µWatt at horizontal position (without rotation angle) and they both have resonance about 13.4 Hz. For a close comparison, a matching diagram is included in Figure 6.28 (a) which match the experiment and theory results for the exactly same

configuration in 45 and 25 degree position. As it can be seen, in theory the amount of power is less than the experiment and as discussed in section 6.1.8 the frequency shift is not being seen in theory and both resonances happen at the same place.

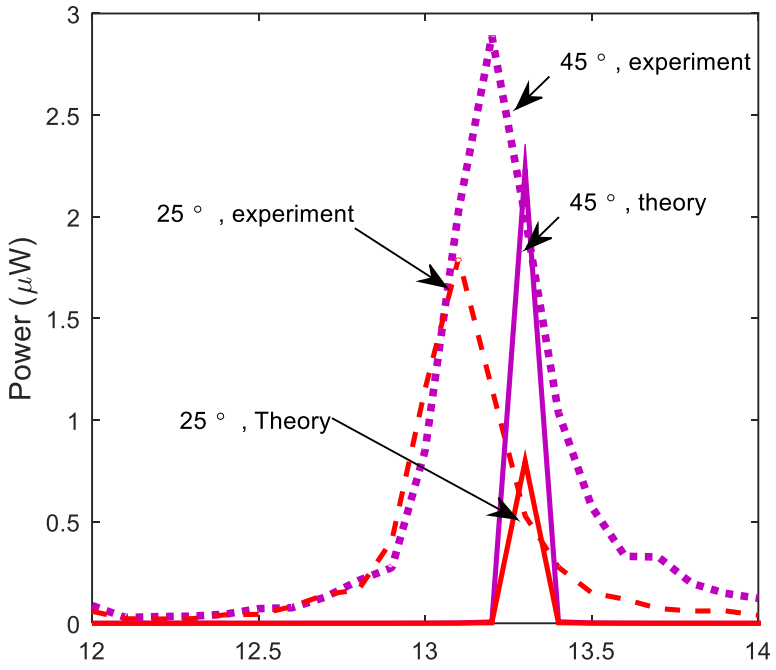

(a) Rotations angles of $\theta = 45^{\circ}, 25^{\circ}$

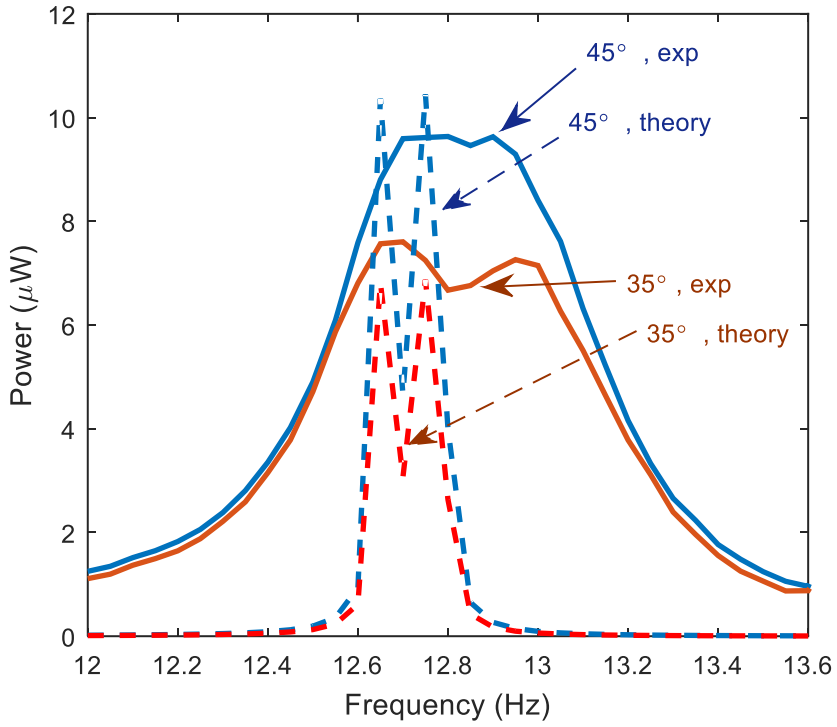

(b) Rotation angle $\theta = 60^{\circ}, 30^{\circ}$

Figure 6.28. Power versus frequency from experiment and theory for two different angles

Also for the mutually perpendicular beams in experimental results of Figure 6.23 and Figure 6.24 a comparison with theoretical results is done in Figure 6.28 (b) where the two approaches are put on each other and the matching of power and frequency are quite good. It is noteworthy to consider that the dimensions of theory and experiment are the same and there is a slight difference in beam length L_{b_1} =249, $L_{b_2} = 250\ mm$, which is considered in both approaches.

6.4. FEM Simulation Results

As discussed in chapter 5, a simulation has been carried out to study the effect of rotation on voltage output and frequency shifting on the piezoelectric beam. The FEM study is carried out both in 2D and 3D model to make sure the integrity of the simulation.

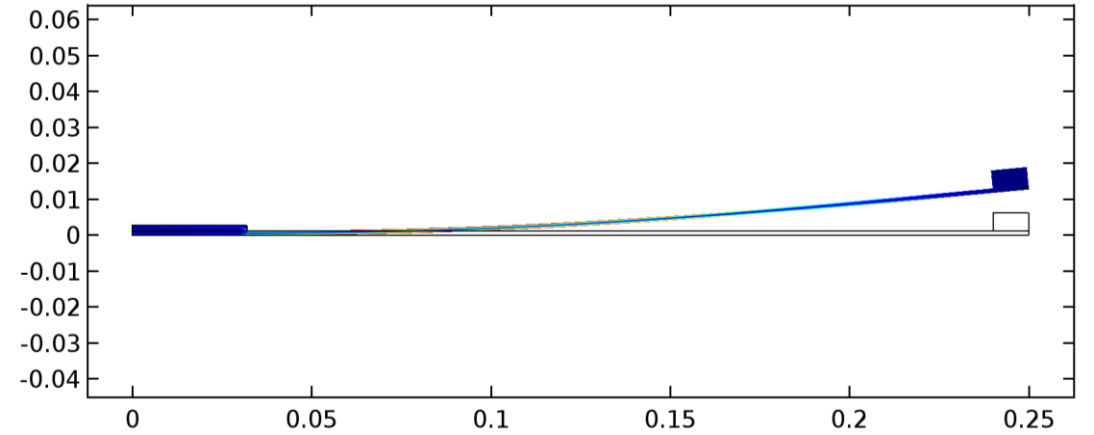

Figure 6.29. 2D FEM static stress analysis simulation of the piezoelectric beam

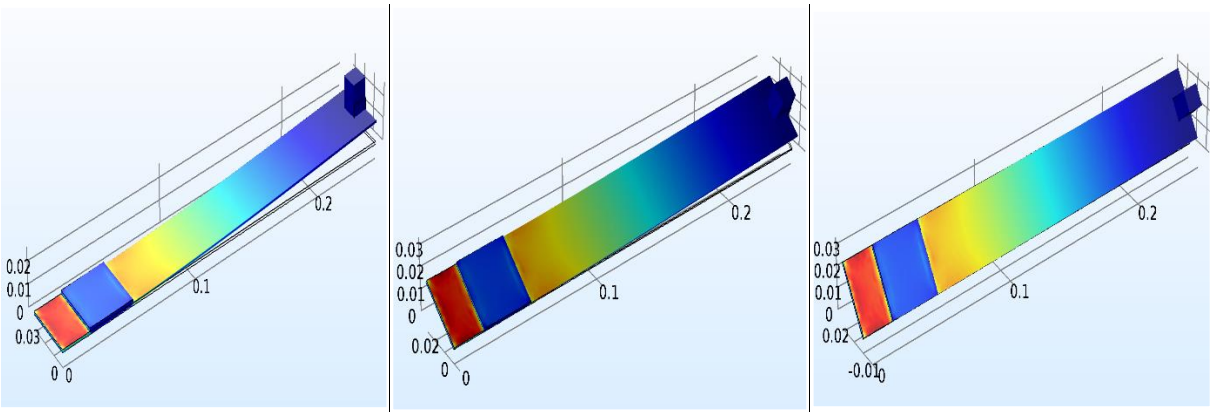

Figure 6.30 .3D FEM static stress analysis of the piezoelectric beam in different angles

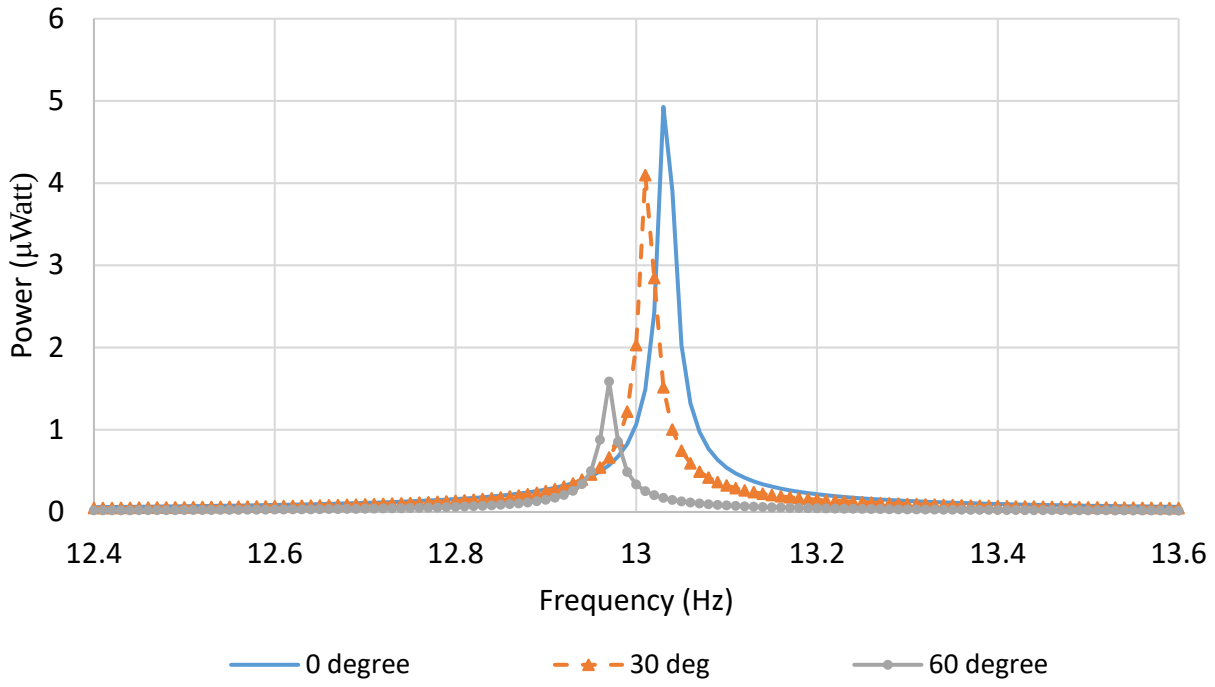

Figure 6.31. FEM result of a single angular piezoelectric beam

As pointed out earlier, the reason for carrying out the simulation is to evaluate the experimental and theoretical results. Figure 6.31 clearly shows a close similarity between power output and resonance frequency of the system. Moreover, by applying a gravity load in the FEM software the frequency shift could be observed which bolster the experimental result in Figure 6.20. The different positions of simulation is also shown in Figure 6.30 to better understand the angular position of the beam like the Figure 6.26 in experiment.

6.5. Comparison of FEM Results with Experiment

The comparison of experiment and simulation is very important since both have minimal error and distance from what is really going to happen for a system if it is undergoing under the predefined initial and boundary conditions.

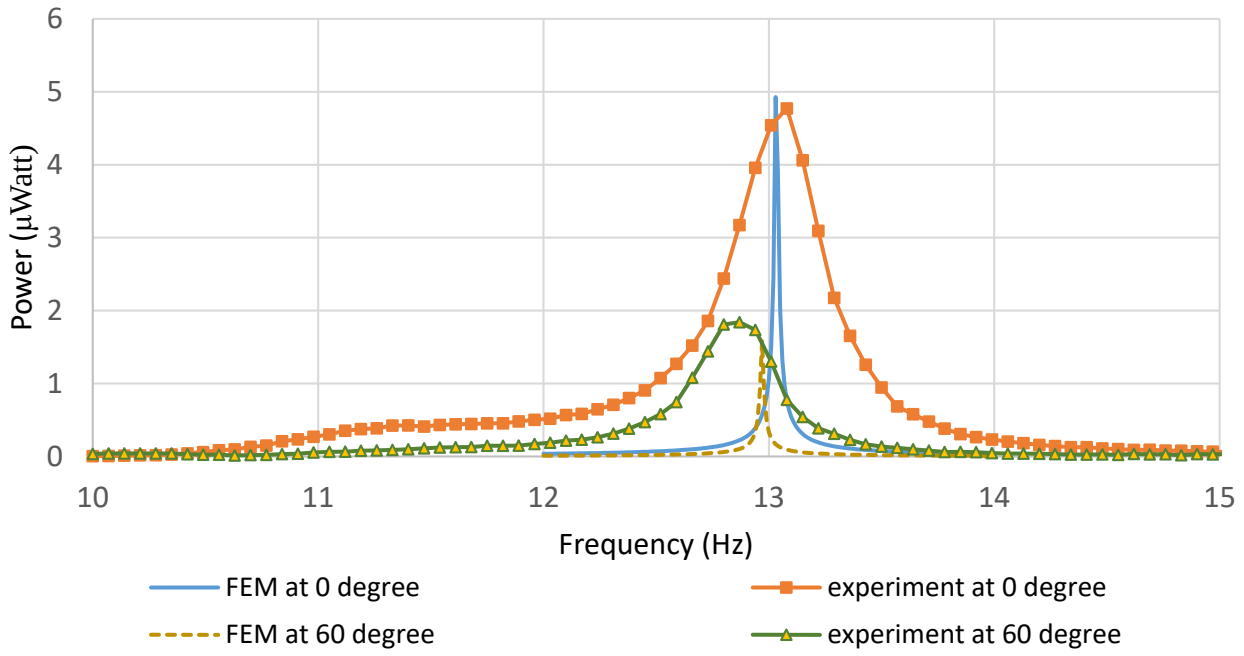

Figure 6.32. Comparison of FEM results with experiment

As it can be seen here, both FEM simulation and experiment have a frequency shift when the rotation angles increases. However, the frequency shift in simulation is less than the experiment but they have a good power resemblance and also the trend in the shifting and power is a correct one and also corroborate the theory.

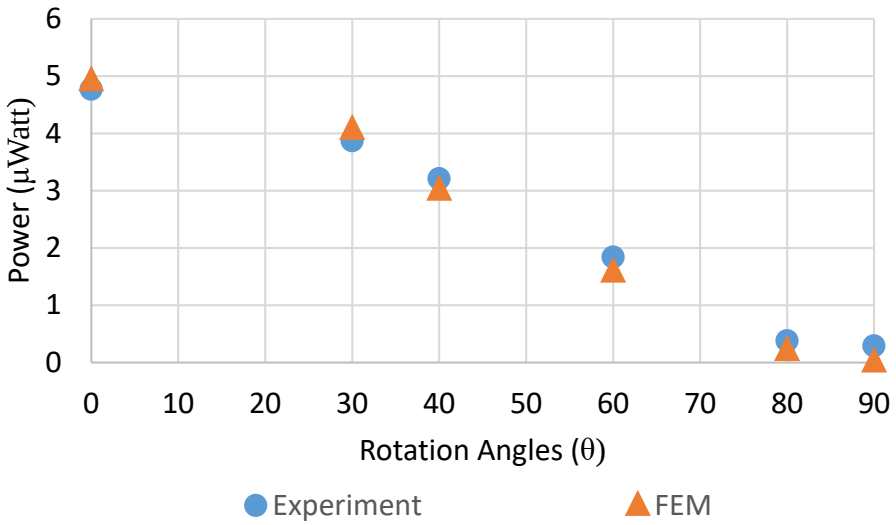

Figure 6.33. Power versus angular position of FEM and Experiment

This figure shows the comparison of experiment and FEM simulation for power versus available tested angles. As it can be seen the power is a little greater in FEM when it is about horizontal position. However, when the beam tilts more, it becomes a little smaller. All in All the three methods here are in a good match with each other and the wider band width is achieved through use of double beam and its length change when the rotation angle changes.

CHAPTER 7

CONCLUSION AND FUTURE WORKS

Three approaches have been carried out to study the effect of angular position about longitudinal axis on power and frequency shift of a mutually perpendicular cantilever single piezoelectric beam. In theoretical results the effect of rotation angle on a single beam shows the decrease of power when the beam tilts. As expected the horizontal beam produces the maximum power because the beam can fluctuate freely. By using another beam in a mutually perpendicular position a wider frequency band is achieved, meaning the harvester can produce power along a greater frequency range. The experimental and FEM simulation results also corroborate the theoretical results. The effect of frequency shift is shown in experiment, both in a single beam case or double beams case. Changing the beam from horizontal to vertical position would lead to a 0.5 Hz frequency change. In finite element method also by changing the beam position likewise a similar shift in frequency is shown and the power decreases accordingly.

The necessity of a reliable power source is a never ending challenge for engineers. Furthermore, piezoelectric materials in spite of being discovered for decades haven't been utilized effectively for energy harvesting. Our research here proved that piezoelectric energy harvester is a good source for power as long as it can be used with in wider bandwidth. Therefore, it is of paramount importance to create and built more innovative ways of increasing the working bandwidth. Additionally, the frequency shift despite our effort did not happen in theory. Therefore, more assiduous work is needed to be done to understand the reason behind this phenomenon.

REFERENCES

1. Singiresu S. Rao. (February 2007). Transverse vibration of beams. *Vibration of continuous systems* (Fourth ed., pp. 317-359) Wiley.

2. Sojan, S., & Kulkarni, R. K. (2016). A comprehensive review of energy harvesting techniques and its potential applications. *International Journal of Computer Applications, 139*(3), 14-19. doi:10.5120/ijca2016909120

3. Thresher, R., Robinson, M., & Veers, P. (2008). Wind Energy Technology: Current Status and R & D Future. *The Physics of Sustainable Energy Conference, University of California at Berkeley*, 24 pp. doi:NREL/CP-500-43374

4. Tang, J., Dai, S., & Darr, J. A. (2012). Recent developments in solar energy harvesting and photocatalysis. *International Journal of Photoenergy, 2012*, 1-2. doi:10.1155/2012/580746

5. Cuadras, A., Gasulla, M., & Ferrari, V. (2010). Thermal energy harvesting through pyroelectricity. *Sensors & Actuators: A.Physical, 158*(1), 132-139. doi:10.1016/j.sna.2009.12.018

6. Anton, S. R., & Sodano, H. A. (2007). A review of power harvesting using piezoelectric materials (2003–2006). *Smart Materials and Structures, 16*(3), R1-R21. doi:10.1088/0964-1726/16/3/R01

7. Xiangdong Xie, Quan Wang, A mathematical model for piezoelectric ring energy harvesting technology from vehicle tires, International Journal of Engineering Science, Volume 94, September 2015, Pages 113-127.

8. G. Gatti, M.J. Brennan, M.G. Tehrani, D.J. Thompson, Harvesting energy from the vibration of a passing train using a single-degree-of-freedom oscillator, Mechanical Systems and Signal Processing, Volumes 66–67, January 2016, Pages 785-792,

9. Y. Tianchen, Y. Jian, S. Ruigang, L. Xiaowei,"Vibration energy harvesting system for railroad safety based on running vehicles" Smart Mater. Struct., 23 (2014), p. 125046

10. J. L. Gonzalez, A. Rubio, and F. Moll, “Human powered piezoelectric batteries to supply power to wearable electronic devices,” Int. J. Soc. Mater. Eng. Res., vol. 10, no. 1, pp. 34-40, 2002.

11. N. S. Shenck and J. A. Paradis, “Energy scavenging with shoe-mounted piezoelectric,” IEEE Micro., vol. 21, no.3, pp. 30-42, 2001.

12. X.D. Xie, Q. Wang, N. Wu, Energy harvesting from transverse ocean waves by a piezoelectric plate, International Journal of Engineering Science, Volume 81, August 2014, Pages 41-48, ISSN 0020-7225.

13. Taufik, T.; Thornton, J.; Dolan, D., "Piezoelectric Converter for Wind Energy Harvesting," in Information Technology: New Generations (ITNG), 2012 Ninth International Conference , vol., no., pp. 221-224, 16-18 April 2012.

14 A. Mehmood, A. Abdelkefi, M.R. Hajj, A.H. Nayfeh, I. Akhtar, A.O. Nuhait, Piezoelectric energy harvesting from vortex-induced vibrations of circular cylinder, Journal of Sound and Vibration, Volume 332, Issue 19, 16 September 2013, Pages 4656-4667.

15. Luo, C., & Hofmann, H. F. (2011). Wideband energy harvesting for piezoelectric devices with linear resonant behavior. IEEE Transactions on Ultrasonics, Ferroelectrics, and Frequency Control, 58(7), 1294–1301. doi:10.1109/TUFFC.2011.1949.

16. Qi, S., Shuttleworth, R., Olutunde Oyadiji, S., & Wright, J. (2010). Design of a multiresonant beam for broadband piezoelectric energy harvesting. Smart Materials and Structures, 19(9), 094009. doi:10.1088/0964-1726/19/9/094009.

17. Yang, Z., & Yang, J. (2009; 2008). Connected vibrating piezoelectric bimorph beams as a wide-band piezoelectric power harvester. *Journal of Intelligent Material Systems and Structures, 20*(5), 569-574. doi:10.1177/1045389X08100042(RW.ERROR - Unable to find reference:2008, RW.ERROR - Unable to find reference:2008, Yang & Yang, 2009; 2008)

18. Ferrari, M., Ferrari, V., Guizzetti, M., Andò, B., Baglio, S., & Trigona, C. (2010). Improved energy harvesting from wideband vibrations by nonlinear piezoelectric converters. *Sensors & Actuators: A.Physical, 162*(2), 425-431. doi:10.1016/j.sna.2010.05.022

19. Erturk, A., & Inman, D. J. (2009). An experimentally validated bimorph cantilever model for piezoelectric energy harvesting from base excitations. *Smart Materials and Structures, 18*(2), 025009. doi:10.1088/0964-1726/18/2/025009

20. Erturk, A., & Inman, D. J. (2008). On mechanical modeling of cantilevered piezoelectric vibration energy harvesters. *Journal of Intelligent Material Systems and Structures, 19*(11), 1311-1325. doi:10.1177/1045389X07085639

21. Alomari, A., & Batra, A. (2015). Experimental and modelling study of a piezoelectric energy harvester unimorph cantilever arrays. *Sensors & Transducers, 192*(9), 37.

22. Wang, K., & Wang, B. (2016). An analytical model for nanoscale unimorph piezoelectric energy harvesters with flexoelectric effect. *Composite Structures, 153*, 253-261. doi:10.1016/j.compstruct.2016.05.104

23. Zhao, J., Yao, F., & Gao, S. (2014). Structure and mechanical analysis of single cantilever piezoelectric energy harvester. *TELKOMNIKA Indonesian Journal of Electrical Engineering, 12*(9) doi:10.11591/telkomnika.v12i9.6012

24. Li, P., Jin, F., & Yang, J. (2013). A piezoelectric energy harvester with increased bandwidth based on beam flexural vibrations in perpendicular directions. *IEEE Transactions on Ultrasonics, Ferroelectrics and Frequency Control, 60*(10), 2214-2218. doi:10.1109/TUFFC.2013.2813

25. Yang, J. S., & Fang, H. Y. (2002). Analysis of a rotating elastic beam with piezoelectric films as an angular rate sensor. *IEEE Transactions on Ultrasonics, Ferroelectrics and Frequency Control, 49*(6), 798-804. doi:10.1109/TUFFC.2002.1009338

26. Li, M., Li, P., Wen, Y., Yang, J., & Dai, X. (2011). A rotation energy harvester employing cantilever beam and magnetostrictive/piezoelectric laminate transducer. *Sensors & Actuators: A.Physical, 166*(1), 102-110. doi:10.1016/j.sna.2010.12.026

27. Abdelkefi, A., Najar, F., Nayfeh, A. H., & Ayed, S. B. (2011). An energy harvester using piezoelectric cantilever beams undergoing coupled bending–torsion vibrations. *Smart Materials and Structures, 20*(11), 115007. doi:10.1088/0964-1726/20/11/115007

28. Jalili, N. (2010). *Piezoelectric-based vibration control from macro to micro/nano scale systems*. New York: Springer Science. doi:10.1007/978-1-4419-0070-8

29. IEEE standard on piezoelectricity. (1996). *Ieee Transactions on Ultrasonics Ferroelectrics and Frequency Control, 43*(5), A1-A54.

30. Jiang, S., Li, X., Guo, S., Hu, Y., Yang, J., & Jiang, Q. (2005). Performance of a piezoelectric bimorph for scavenging vibration energy. *Smart Materials and Structures, 14*(4), 769-774. doi:10.1088/0964-1726/14/4/036

31. Holland, R., & EerNisse, E. P. (1969). Design of Resonant Piezoelectric Devices; Research Monograph 56.Chicago